

# Models for Fracture during Deformation Processing

Howard Kuhn, The Ex One Company

IN VERY BROAD TERMS, MODELING OF FRACTURE DURING DEFORMATION PROCESSES has been a major focal point for production engineers since cracking first occurred as a source of scrap in manufacturing. G. Sachs, in his 1954 compilation of articles in *Fundamentals of the Working of Metals* (Ref 1), pointed out that “Two characteristics of any metal or alloy are of particular interest to the engineer engaged in the working of metals. The one is the ability of the metal to withstand permanent or plastic changes in shape or deformations, and it is called ductility. . . The other metal property of interest to the processing engineer is the resistance of the metal to deformation. . . For any given material to be processed, both the ductility and the deformation resistance may differ with the variables of processing within very wide limits.” In other words, it was recognized early on that the plastic deformation and fracture behavior of materials were functions not only of the material but the processing conditions as well.

## Background

At that time, ductility was primarily expressed through measurements of elongation and reduction of area in a tension test. Ongoing testing and everyday experience illustrated that the ability of a metal to tolerate deformation without fracture was usually enhanced by increasing temperature and by decreasing rate of deformation. It was also recognized that ductility was strongly dependent on the size and amount of particles or precipitates dispersed throughout the material. Increasing volume fraction of particles drastically reduces tensile ductility (Ref 2) by providing sources for void initiation, which then grow and coalesce into cracks with increasing plastic deformation.

Process engineers further understood that tensile stresses, or better yet, hydrostatic tension, played a strong role in fracture during metalworking processes. Pioneering work by Bridgman (Ref 3) during WWII showed that deforming materials under high superimposed

hydrostatic pressure dramatically enhanced their ductility, so it was presumed that hydrostatic tension would have the opposite effect. It was further recognized that secondary tensile stresses occur in generally compressive processes, such as the hoop stress due to barreling in axial compression of a cylinder. However, plasticity theory was in its infancy and not yet available in convenient form for everyday practitioners to determine the detailed stress and strain conditions throughout a workpiece undergoing practical metalworking operations.

Early “models” of fracture in metalworking processes assembled these data for a given material, which was expressed through:

- Tabulations (both mental and on paper) of the ranges of temperature and deformation rate at which cracking was likely
- Sketches of crack locations in various processes (Fig. 1), with guidelines (again, both mental and on paper) on their prevention

Experience-based knowledge was the foundation of predictive models for process design to avoid defects. Today (2009), such experience-based knowledge is supplemented by analytical methods using models of fracture to provide a more reliable approach to troubleshooting fracture problems in processes, or to design a process to avoid fracture.

**Physical modeling** of processes, using soft materials such as plasticene (nonhardening clay) or lead, became popular in the evolution of plasticity analysis. Grid lines were placed on the model material, which was then formed by low-cost tooling that represented the actual process of interest. The deformed grid lines then revealed the pattern of deformation and strains occurring at various points throughout the workpiece. Compressed plasticene cylinders with internally gridded meridian planes were used to determine the degree of inhomogeneity due to various lubrication conditions (Ref 4, 5), and lead billets with internally gridded planes were used to understand the inhomogeneity of

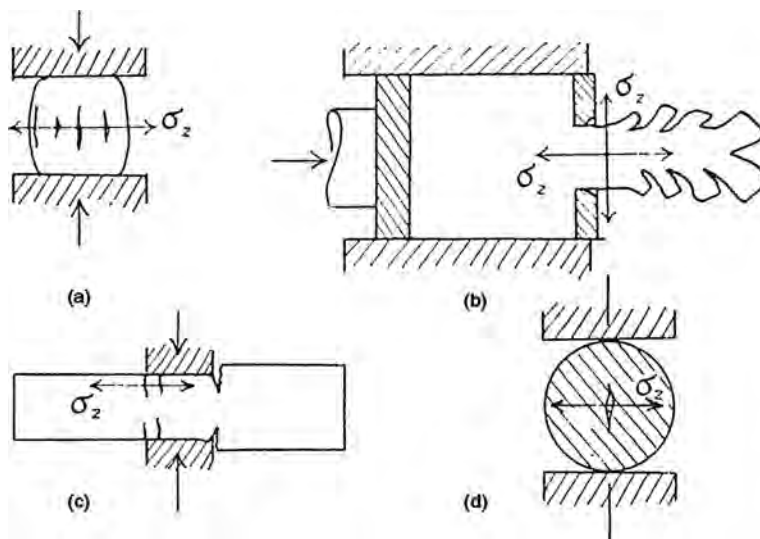


Fig. 1 Sketches of processing defects form a basis for early models. (a) Forging or compression test specimen. (b) Extrusion. (c) Drawing. (d) Forging with no horizontal constraint at die surface Source: Ref 1

plastic deformation during open-die forging and rolling (Ref 6) and extrusion (Ref 7). Plasticene and copper specimens with grid lines were used to interpret the complex distribution of strains in shear spinning (Ref 8). Plasticene with small, embedded metal cylinders has also been used to visualize the localized deformation around inclusions leading to void initiation, growth, and coalescence in ductile fracture (Ref 9). Translation of the strain measurements into stress distributions was accomplished by development of the viscoplasticity method. Measured grid displacements were first transformed into strain-field calculations, and the Levy-Mises

plasticity equations were then used to calculate the accompanying stress fields (Ref 10). This method proved tedious but did provide some important insights into the critical stresses in the vicinity of crack formation. Modern tools for digitizing images would streamline the viscoplasticity method today, but its use is superseded by computerized finite-element analytical methods, as discussed later.

The slab method of analysis is of little help in modeling fracture during plastic deformation processes because it considers deformation to be homogeneous through the thickness of the workpiece, and it is clear that nonuniformity of

deformation is a key ingredient leading to stress states favorable to fracture. Nevertheless, the method has been used to interpret fracture conditions during compression of fiber-reinforced composite plates (Ref 11). As shown in Fig. 2, compression of a composite plate (25 vol% stainless steel wire in a 6061 aluminum matrix) perpendicular to the fiber direction leads to void formation around the fibers near the plate ends. During compression of a plate, the lateral pressure,  $q$ , and normal pressure,  $p$ , increase toward the lateral central axis of the plate (Fig. 3); the rate of increase depends on the lumped parameter  $\mu L/h$ , where  $\mu$  is the coefficient of friction, and  $L$  and  $h$  are the instantaneous length and height of the plate. Comparing the lateral positions of the voids with the local stresses calculated by the slab method, the ratio of lateral pressure to vertical pressure,  $q/p$ , required to prevent void formation was calculated. Figure 4 shows the

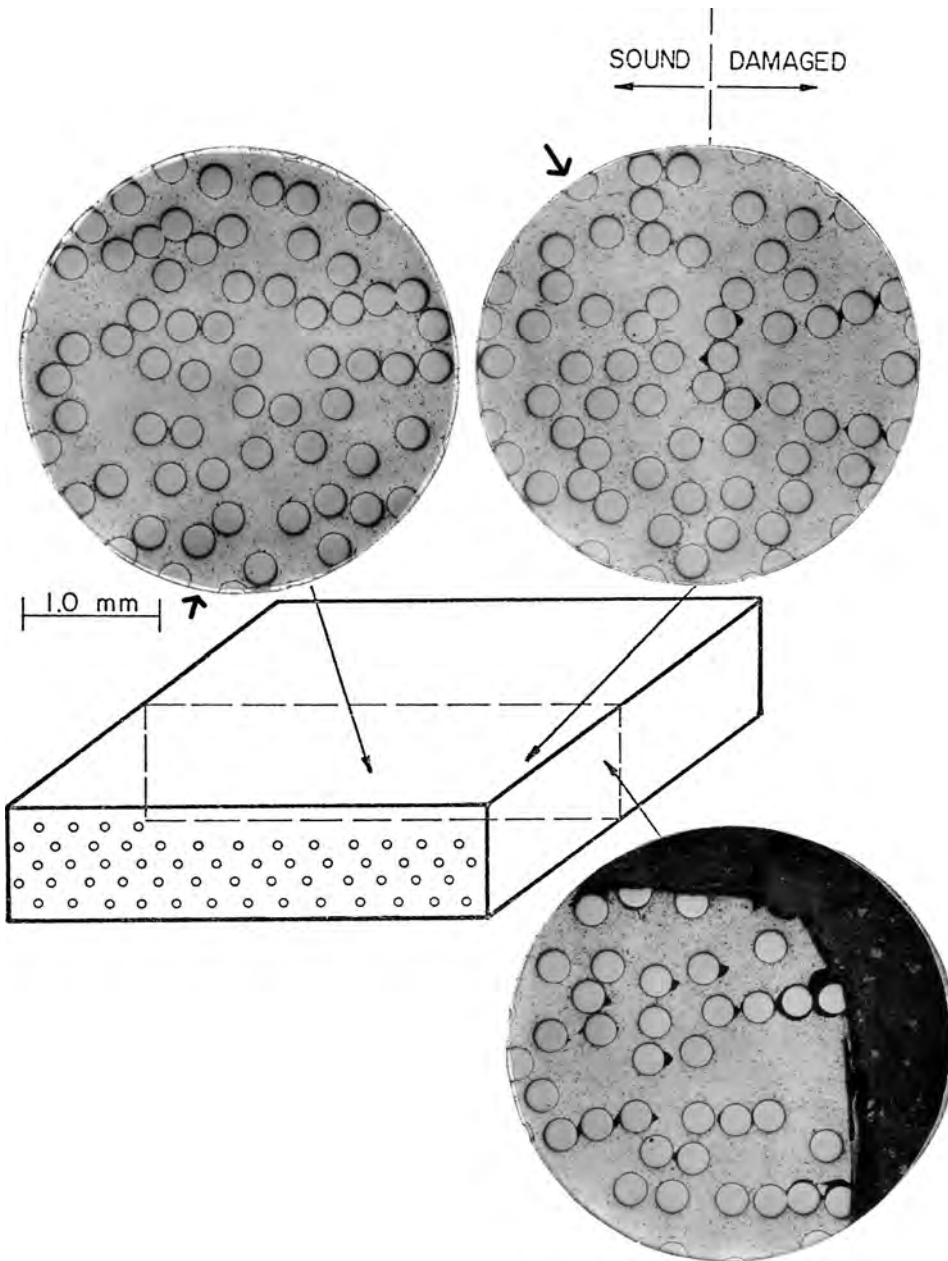


**Fig. 2** Macrographs of the polished mid-plane of a composite plate compressed to 50% reduction in height. The innermost evidence of void formation around reinforcing fibers delineates between sound and damaged material. Matrix is 2024 aluminum alloy with 25 vol% NS355 stainless steel wire (0.23 mm diameter) reinforcement. Plates are 6.4 mm thick, 12.7 mm wide and variable length from 6.4 to 19.0 mm. Source: Ref 11

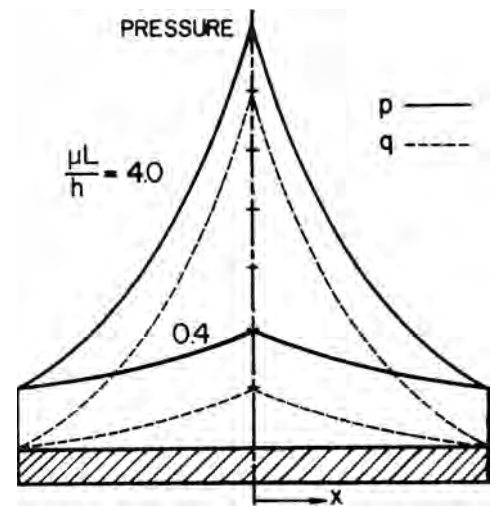


**Fig. 3** Distribution of vertical forming pressure,  $p$ , and lateral internal pressure,  $q$ , in the lateral direction for two different values of  $\mu L/h$ . Source: Ref 11

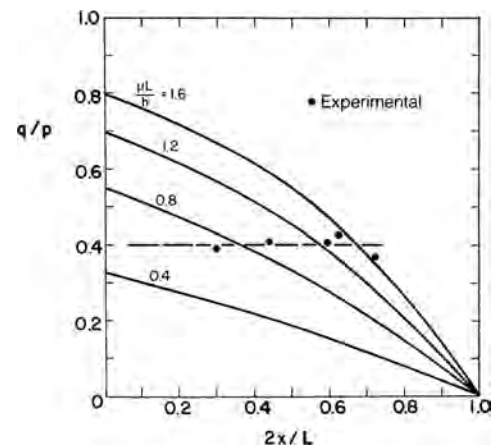


**Fig. 4** Values of calculated local lateral pressure to axial pressure ratio ( $q/p$ ) at measured positions of the transition between sound and damaged material in compressed composite plates of various geometries at 20% reduction in height. Source: Ref 11

experimental results for 20% compression and various forging parameters  $\mu L/h$ . Repeating the tests for various degrees of compression, a forming limit was determined for the composite (Fig. 5).

The upper-bound method of analysis was developed primarily to provide a quick determination of the pressures required in various metalforming operations (Ref 12). Based on equating the external work done to the energy dissipated by an assumed flow field in the workpiece, its first manifestation considered rigid rectangular, triangular, or trapezoidal blocks separated by lines of velocity discontinuity. The method involves searching for the pattern of blocks to represent metal flow that minimizes the overall deformation energy and thus the forming load. While the method is not useful in determining localized stresses for prediction of crack formation, it can be used to determine the process conditions likely to produce defects. Johnson and Kudo (Ref 13) showed that in a double forging/extrusion operation, a flow field that assumed cavity formation at the centerline (known as central burst) would lead to the lowest forming load under certain geometric conditions (Fig. 6). Avitzur (Ref 14) later extended the upper-bound method by using continuous functions to

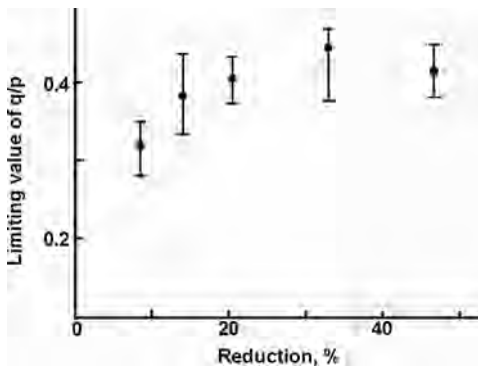


Fig. 5 Forming limit in terms of the limiting pressure ratio  $q/p$  to prevent void formation as a function of height reduction. Source: Ref 11

represent the flow field and applying optimization techniques to determine the flow functions that minimize the energy of dissipation. Perturbations can be incorporated in the flow functions to simulate defect formation. In some situations, the external work required to create the flow field with defects is lower than the work required for sound flow, as shown in Fig. 7 for wiredrawing. The calculated external load (drawing force) is plotted along the vertical axis as a function of die half-angle. For angles less than  $\alpha_1$ , sound flow occurs, and for angles greater than  $\alpha_2$ , sound flow occurs with a dead-metal zone forming at the die. Between these two limits, however, a flow field allowing for central burst formation requires a lower load than either of the sound flow modes. Therefore, in this range of die angles, a necessary condition for central burst cracking is satisfied. Repeated calculations using the

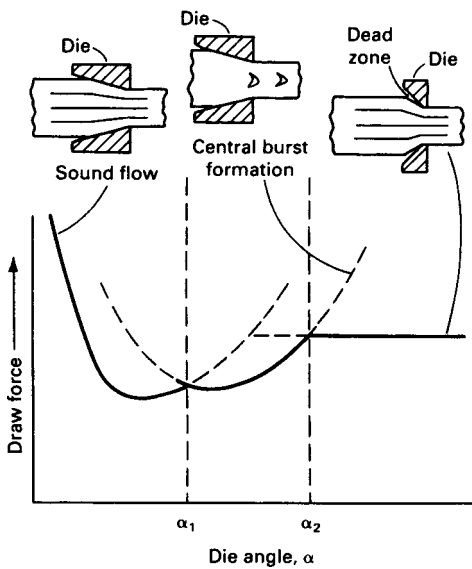


Fig. 7 Drawing force as a function of die half-angle. Central burst formation requires lower external applied load than sound flow in the region between  $\alpha_1$  and  $\alpha_2$ . Source: Ref 25

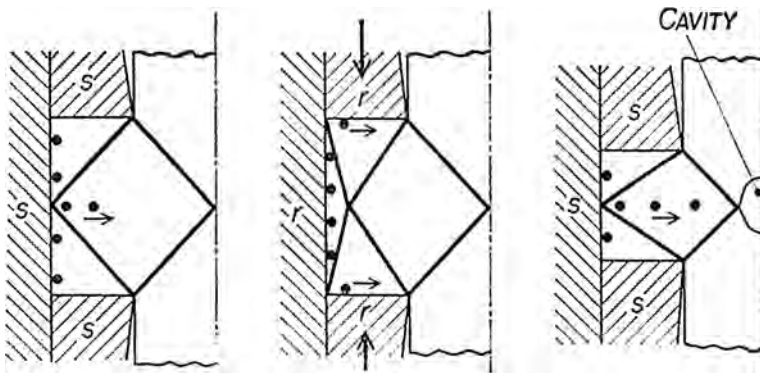


Fig. 6 Upper-bound analysis of a double extrusion-forging process showing sound flow on the left and cavity formation at the centerline on the right. Source: Ref 13

upper-bound method provide the combinations of die angle and reduction that cause central burst (Fig. 8) for various  $m$  factors ( $0 < m < 1.0$ ) representing friction along the die surfaces. For a given value of friction, internal cracking is predicted to occur for die angle and reduction combinations below the line, and no defects occur above the line. Note that, for a given die angle, one approach to avoid central burst is to increase the reduction! This example is a clear illustration of the role of process parameters (in this case, geometric conditions) in the occurrence of fracture. It should be repeated that the upper-bound method for defect prediction gives only a necessary condition. The strain-hardening and strain-rate-hardening characteristics of the material can be included in the analysis, but the material microstructural characteristics are not included. Therefore, when operating in the central burst range illustrated in Fig. 8, fracture can occur; whether or not it will occur depends on the material structure (voids, inclusions, segregation, etc.). Experimental validation of the forming limits in Fig. 8 showed that, of 500 extrusions in the central burst zone, 4.5% of the parts had central burst, while none of 500 extrusions in the safe zone showed central burst (Ref 17).

Slip-line field analysis provides a geometric method for calculation of stress states in plastic deformation processes, particularly the hydrostatic stress state. While strictly applicable only to non-work-hardening material and plane-strain deformation, the method provides useful insight into the role of deformation process geometric conditions on the potential for fracture and its location in the workpiece. For example, double indentation by flat punches is a classical problem in slip-line field analysis, illustrated in Fig. 9 for various ratios of

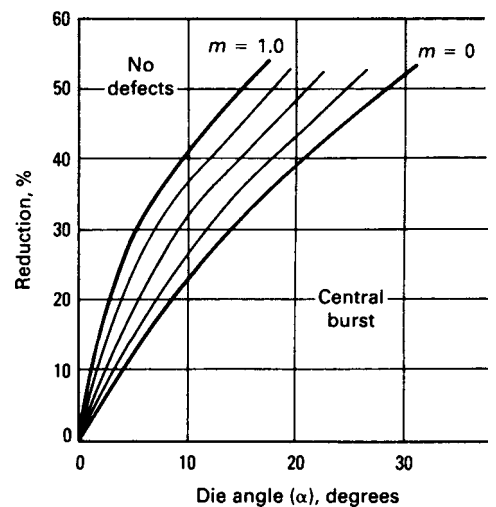


Fig. 8 Upper-bound prediction of central burst in wire drawing in terms of reduction and die half-angle. Increasing friction, expressed by the friction factor,  $m$ , increases the defect region of the map. Source: Ref 25

workpiece height to punch width,  $h/b$ . Boundaries of the deformation zone change as  $h/b$  increases. For  $h/b < 1$ , the deformation region is spread over an area nearly as large as the punch width. When  $h/b > 1$ , the deformation zone meets the centerline at a point. For any configuration, the punch pressure and the hydrostatic stress at the centerline can be calculated by traditional slip-line field analysis (Ref 19). Figure 10 shows that both punch pressure and centerline hydrostatic stress increase with increasing  $h/b$ . The critical geometry is  $h/b = 1.8$  because the hydrostatic stress becomes tensile for  $h/b$  ratios greater than this value. The tooling arrangement and deformation geometry in Fig. 9 approximates several other metalworking processes, including rolling, drawing/extrusion, and open-die forging (Fig. 11). For similar  $h/b$  ratios in these processes, the stresses throughout the deformation zone can be approximated by those calculated

from slip-line analysis for double indentation. The results of slip-line field analysis for double indentation can be applied to prediction of central burst in drawing and extrusion. For example, in extrusion or drawing,  $h/b$  is approximated by:

$$h/b = \alpha[1 + (1 - R)^{1/2}]^2 / R \quad (\text{Eq 1})$$

where  $\alpha$  is the die half-angle, and  $R$  is the area reduction. Taking  $h/b = 1.8$  as the critical ratio at which the centerline hydrostatic stress becomes tensile, the relationship between  $\alpha$  and  $R$  can be calculated. The result is shown in Fig. 12 along with the similar relationship predicted by the upper-bound analysis (Fig. 8). The correlation is remarkable in view of the dissimilarity in die shape between extrusion and double indentation. The similarity in results shown in Fig. 12 indicates that the flow mode for defect formation in the upper-bound method

is physically equivalent to the development of tensile hydrostatic stress at the centerline. The use of slip-line field analysis for fracture modeling was also used in the classic study by Coffin and Rogers (Ref 20). Slip-line field analysis of sheet drawing was used in combination with very carefully executed experiments on

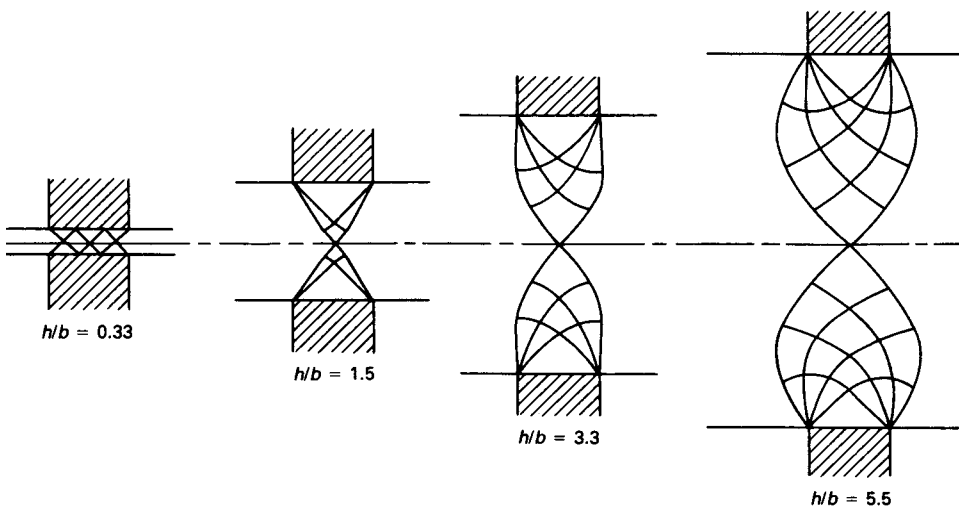


Fig. 9 Slip-line fields for double indentation at various ratios of workpiece height to punch width,  $h/b$ . Source: Ref 25

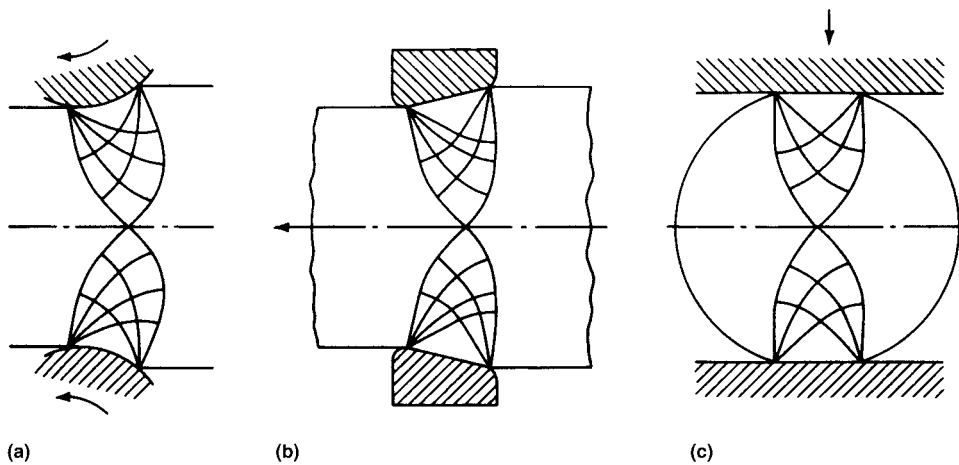


Fig. 11 Slip-line fields for (a) rolling, (b) drawing, and (c) side pressing. These fields are similar to those for double indentation of a thick slab shown in Fig. 9.

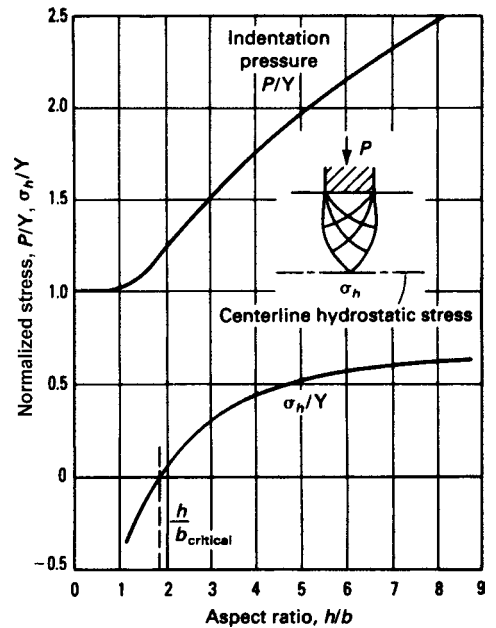


Fig. 10 Variation of the normalized indentation pressure ( $P/Y$ , where  $Y$  is the yield strength) and the normalized centerline hydrostatic stress ( $\sigma_h/Y$ ) with  $h/b$  ratio as calculated from slip-line field analysis. Source: Ref 25

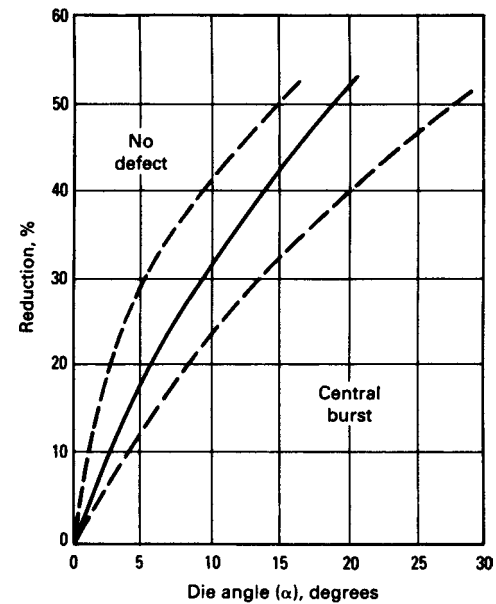
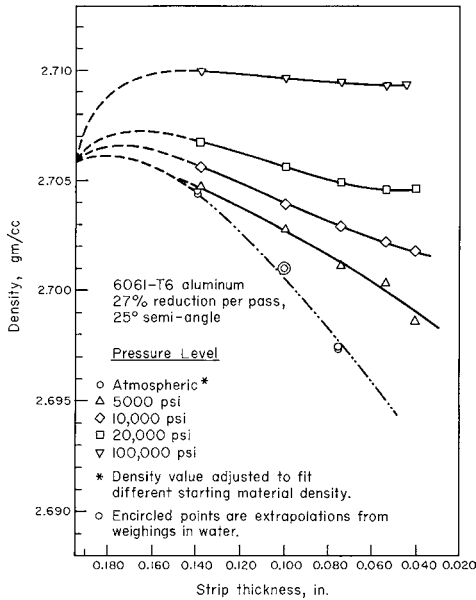


Fig. 12 Prediction of central burst in wire drawing by the tensile stress criterion and slip-line field analysis (solid line) of double indentation. The range of predictions by upper-bound analysis (Fig. 8) is shown by dashed lines. Source: Ref 25

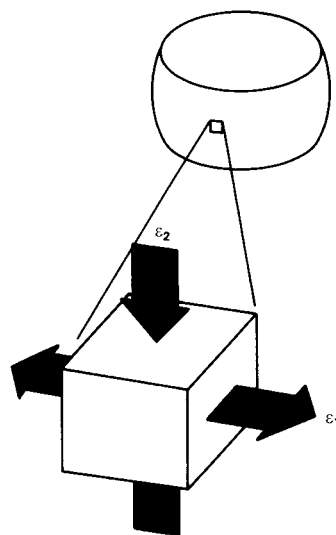
various copper alloys, followed by extensive optical metallography. Results showed that hydrostatic tension at the centerline exclusively led to void formation and slight density reduction, while hydrostatic compression led to zero or slight density increase (Fig. 13).

### Fracture Criteria

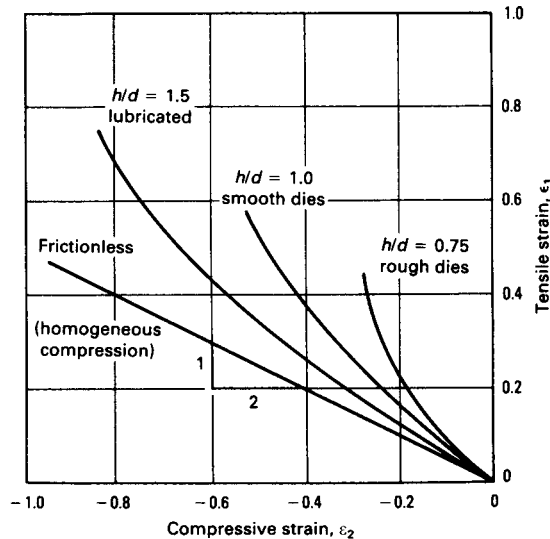
The fracture models described previously, while providing useful insights, are approximate in their determination of the process or material



**Fig. 13** Density of 6061-T6 aluminum alloy drawn under different externally applied hydrostatic pressures as a function of thickness. Nominal 27% reduction per pass with die half-angle of 25°. Source: Ref 17



(a)



(b)

**Fig. 14** Localized strains on (a) the bulging cylindrical surface of an upset test and (b) their variation with aspect ratio and friction conditions. Source: Ref 34

conditions leading to fracture. They rely primarily on the expectation that hydrostatic tension is the major culprit leading to fracture but do not address the role of any material characteristics.

Modern finite-element analytical techniques have advanced in four decades from simple linear structures to nonlinear rigid-plastic analysis to elastic-plastic analysis of anisotropic, work-hardening, strain-rate-sensitive materials in complex three-dimensional, large-strain processes. As a result, they are capable of providing detailed, fine-granularity maps of all components of the stress and strain tensors and their combinations, as well as scalar temperatures and their vector gradients, throughout the history of a deformation process. Accurate prediction of fracture during metalworking processes, then, should be accomplishable by inserting a criterion of fracture that faithfully represents the behavior of the material of interest.

**General observations** of ductile fracture in metalworking can be distilled to two universal conclusions:

- Tensile stress and plastic deformation constitute necessary ingredients for fracture, and control of these localized conditions through modification of the global process parameters (die geometry, workpiece geometry, and friction) can restrain the occurrence of fracture (Ref 1, 3, 11, 13, 20–24).
- Ductile fracture involves the generation, growth, and coalescence of voids, and this sequence of events is dependent on the microstructure and deformation mechanisms prevalent in the material, as well as the localized conditions of stress and deformation (Ref 1, 2, 25–27).

A criterion of fracture for use in finite-element analyses should include these effects implicitly, if not explicitly.

A suitable validation standard should be established for evaluation of the various criteria. Tension testing is not suitable because it produces one basic stress state rather than the variety experienced in metalforming operations. The upset test on cylinders, on the other hand, can generate a variety of stress states on its cylindrical surface through changes in workpiece geometry and interface friction conditions. In addition, a wealth of information is available on this test through research by a number of investigators (Ref 28–33).

**Upset compression testing** has become a standard for workability evaluation. As shown in Fig. 14, a range of strain combinations can be developed at the cylindrical free surface simply by altering friction and geometry conditions. The influence of friction and consequent bulging on circumferential tensile stress development is clearly shown in Fig. 15. Compression with friction produces circumferential tension that leads to fracture, while frictionless compression prevents barreling, tension, and cracking. Stresses at the cylindrical surface of the upset cylinder are related to the surface strains by:

$$\begin{aligned} \sigma_1 &= \frac{4}{3}\lambda[\epsilon_1 + \frac{1}{2}\epsilon_2] \\ \sigma_2 &= \frac{4}{3}\lambda[\epsilon_2 + \frac{1}{2}\epsilon_1] \end{aligned} \quad (\text{Eq 2})$$

where  $\lambda = \bar{\epsilon}/\bar{\sigma}$  is the ratio of effective strain to effective stress. For frictionless (homogeneous) compression,  $\epsilon_1 = -\frac{1}{2}\epsilon_2$ , so the circumferential stress  $\sigma_1$  is zero. That is, for frictionless compression, the stress state is purely compressive (i.e.,  $\sigma_2 = -Y$ , the material flow stress), and the hydrostatic stress is  $-Y/3$ . For larger absolute ratios of strain, the localized circumferential stress becomes more tensile, while the axial compressive stress becomes less compressive.

Alterations of the compression test geometry have been devised to extend the range of surface strains available toward the vertical, tensile test specimens. Test specimens are essentially prebulged by machining a taper or a flange on the cylinders (Fig. 16). Compression then causes lateral spread of the interior material, which expands the rim circumferentially while applying little axial compression to the rim. Therefore, the tapered and flanged upset test specimens provide strain states consisting of small compressive strain components. Each combination of height,  $h$ , and thickness,  $t$ , gives



**Fig. 15** Compression tests on 2024-T35 aluminum alloy. Left to right: Undeformed specimen, compression with friction (cracked), compression without friction (no cracks)

a different ratio of tensile to compressive strain. The strain states developed at the surfaces of straight, tapered, and flanged compression test specimens are summarized in Fig. 17.

The variety of strain combinations available in compression tests offers the possibility for material testing over most of the strain combinations that occur in actual metalworking processes. A number of samples of the same material and condition are tested, each one under different friction and geometry parameters. Tests are carried out until fracture is observed, and the local axial and circumferential strains are measured at fracture. Figures 18 to 20 give some examples of results for AISI and SAE 1045 carbon steel, 2024-T351 aluminum alloy at room temperature, and 2024-T4 alloy at a hot-working temperature (Ref 28). In some cases, the fracture strains fit a straight line of slope  $-1/2$ ; in others, the data fit a dual-slope line with slope  $-1/2$  over most of the range and slope  $-1$  near the tensile strain axis. Similar data have been obtained for a wide variety

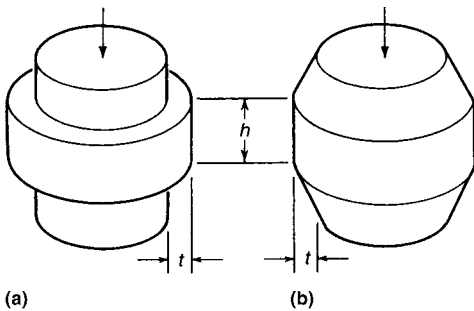


**Fig. 16** Depiction of (a) flanged and (b) tapered prebulged compression test specimens. Lateral spread of interior material under compression expands the rim circumferentially while little axial compression is applied (see Fig. 17).

of materials. In each case, the straight-line behavior (single or dual slope) appears to be characteristic of all materials, but the height of the line varies with the material, its microstructure, test temperature, and strain rate. Similar results have been found, initially by Kudo and Aoi (Ref 29), Kobayashi (Ref 30), Thomason (Ref 31), Ganser et al. (Ref 32), and Bao and Wierzbicki (Ref 33).

The nature of the fracture loci shown in Fig. 18 to 20 suggests an empirical fracture criterion representing the material aspect of workability. The strain paths at potential fracture sites in material undergoing deformation processing (determined by measurement or mathematical analysis) can then be compared to the fracture strain loci. Such strains can be altered by process parameter adjustment, and they represent the process input to workability. If the

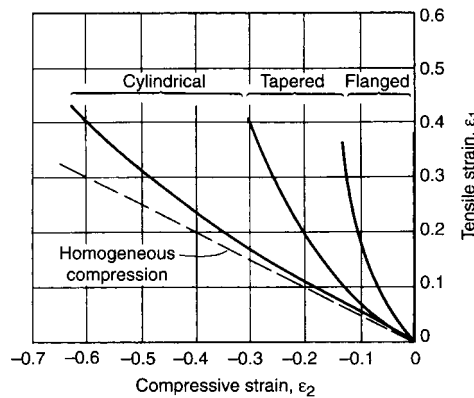


**Fig. 17** Range of free surface strain combinations for compression tests having cylindrical (Fig. 14), tapered, and flanged (Fig. 16) edge profiles. The ranges shown are approximate, and they may overlap a small amount.

process strains exceed the fracture limit lines of the material of interest, fracture is likely.

**Fracture models** have been devised in an attempt to derive a fracture criterion. Most models are based on the concept of void nucleation and growth to coalescence along bands of high shear stress, as depicted in Fig. 21, originally developed by McClintock (Ref 35) and later by Rice and Tracey (Ref 36). Figure 22 shows a plot of the predicted strain locus at fracture by the McClintock model. The predicted fracture strain line has a slope of  $-1/2$  over most of its length, matching that of the experimental fracture line. Near the tensile strain axis, the slope of the predicted line is  $-1$ , matching that of actual material results shown in Fig. 19 and 20.

In sheet forming, the observation that a neck forms before fracture, even under biaxial stress conditions in which localized instability cannot occur, has prompted consideration of the effects of inhomogeneities in the material. For example, a model of localized thinning due to a small inhomogeneity has been devised (Ref 37). Beginning with the model depicted in Fig. 23, plasticity mechanics is applied to determine the rate of thinning of the constricted region,  $t_B$ , in relation to that of the thicker surrounding material,  $t_A$ , in region A. When the rate of thinning reaches a critical value, the limiting strains are considered to have been reached, and a forming-limit diagram can be constructed. The analysis includes the effects of crystallographic anisotropy, work-hardening rate, and inhomogeneity size,  $t_B/t_A$ .

**The R-Z-Models.** The Marciniak Kuczynski model (Ref 37) was applied to free surface fracture in bulk-forming processes because of evidence that localized instability and thinning also precede this type of ductile fracture (Ref 38). Two model geometries were considered, one having a groove in the axial direction (Z-model) and the other having a groove in the radial direction (R-model), as shown in Fig. 23. Applying plasticity mechanics to each model, fracture is considered to have occurred when the thin region B,  $t_B$ , reduces to zero thickness. When the fracture strains are plotted for different applied stress ratios, a fracture strain line can be constructed. As shown in Fig. 24, the predicted fracture line matches the essential features of the experimental fracture lines (Fig. 18 to 20). The slope is  $-1/2$  over most of the strain range and approximately  $-1$  near the tensile strain axis.

For both the R- and Z-models shown in Fig. 23, the applied strain ratio during any increment of deformation will be defined as:

$$K = -d\epsilon_z / d\epsilon_\theta \quad (\text{Eq 3})$$

This gives an increment in equivalent strain in region A, the matrix material:

$$d\bar{\epsilon}_A = d\epsilon_\theta (2/\sqrt{3})(1 - K + K^2)^{1/2} \quad (\text{Eq 4})$$

and an applied stress ratio, from the Levy-Mises equations, of:

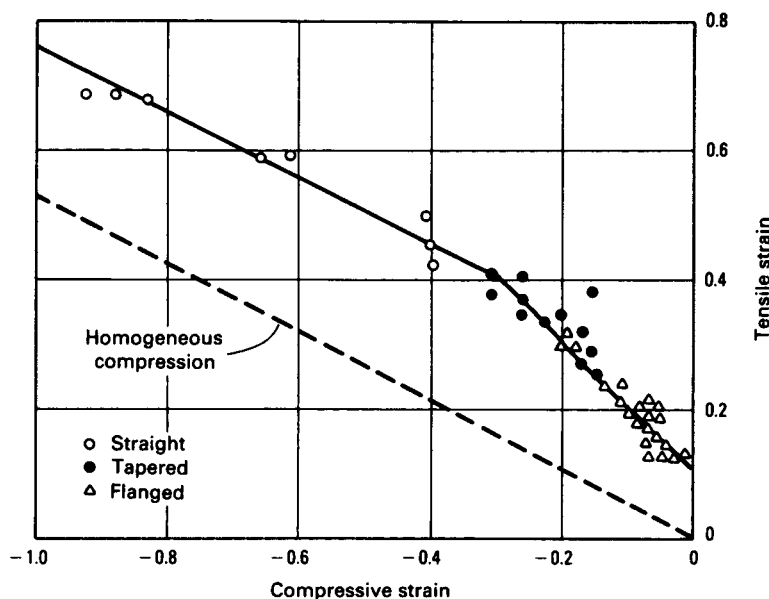


**Fig. 18** Fracture locus for AISI 1045 cold-drawn steel

$$r = \sigma_{zA} / \sigma_{\theta A} = (2K - 1) / (K - 2) \quad (\text{Eq 5})$$

The equivalent stress in region A is then:

$$\bar{\sigma}_A = \sigma_{\theta A} (1 - r + r^2)^{1/2} \quad (\text{Eq 6})$$

The radial stress is taken to be zero because each model applies to an element at or near the surface.

In region B, the groove, equilibrium gives:

$$\sigma_{\theta B} = \sigma_{\theta A} (t_A / t_B) = \sigma_{\theta A} / f \quad (\text{Eq 7})$$

where  $f = t_B / t_A$

Assuming  $\sigma_z$  is the same in regions A and B:

$$\sigma_{zB} / \sigma_{\theta B} = (\sigma_{zA} / \sigma_{\theta A}) f = rf \quad (\text{Eq 8})$$

then the equivalent stress in region B is:

$$\bar{\sigma}_B = \sigma_{\theta B} (1 - rf + r^2 f^2)^{1/2} \quad (\text{Eq 9})$$

Now combining Eq 6, 7, and 9:

$$\bar{\sigma}_B = \bar{\sigma}_A [(1 - rf + r^2 f^2) / (1 - r + r^2)]^{1/2} / f \quad (\text{Eq 10})$$

Using the relation between equivalent stress and equivalent strain,  $\bar{\sigma} = C \bar{\epsilon}^n$ , the equivalent stress in Eq 10 is eliminated, giving:

$$\bar{\epsilon}_B = \bar{\epsilon}_A \{ [(1 - rf + r^2 f^2) / (1 - r + r^2)] / f^2 \}^{1/2n} \quad (\text{Eq 11})$$

Evaluating Eq 11 for each increment in deformation gives  $d\bar{\epsilon}_B$ , the increment of effective strain in region B. Then, from the Levy-Mises equations, the incremental strains in region B are:

$$d\bar{\epsilon}_{\theta B} = d\bar{\epsilon}_B (1 - rf/2) / (1 - rf + r^2 f^2)^{1/2} \quad (\text{Eq 12})$$

$$d\epsilon_{zB} = d\bar{\epsilon}_B (rf - 1/2) / (1 - rf + r^2 f^2)^{1/2} \quad (\text{Eq 13})$$

$$d\epsilon_{rB} = d\bar{\epsilon}_B (-rf/2 - 1/2) / (1 - rf + r^2 f^2)^{1/2} \quad (\text{Eq 14})$$

The change in thickness ratio,  $f = t_B / t_A$ , for the R-model is given by:

$$df = f (d\epsilon_{zB} - d\epsilon_{zA}) \quad (\text{Eq 15})$$

and for the Z-model:

$$df = f (d\epsilon_{rB} - d\epsilon_{rA}) \quad (\text{Eq 16})$$

This prescribes a new value of  $f$ , which, along with the appropriate value of  $K$ , is used to calculate the strains for a new increment of deformation using Eq 12 to 14.

It can be expected that the R-model will lead to thinning of the groove for any value of  $K < 2.0$ , because the resulting tensile stress,  $\sigma_{\theta}$ , will produce greater thinning than would naturally occur under the axial compressive stress,  $\sigma_z$ . At  $K = 2.0$ , no circumferential tensile stress occurs, and both regions A and B thin the same amount under the axial stress ( $df = 0$ ).

The Z-model will lead to thinning for  $0 \leq K < 1.0$ . In this domain,  $\sigma_{\theta}$  is greater than  $|\sigma_z|$ , and the Poisson contraction in the radial direction in the groove due to tensile stress,  $\sigma_{\theta}$ , will be greater than the Poisson extension due to compressive stress,  $\sigma_z$ . At  $K = 1.0$ , these effects balance so that no thinning occurs, and for  $K > 1.0$ , the groove increases in thickness more rapidly than the matrix ( $df > 0$ ).

The calculation procedure for the model of localized thinning is relatively simple and

can be used to give the strains and  $f$ -value explicitly. Calculations in this study were performed on a programmable desk-top electronic calculator. A typical result of the variation of  $f$  during deformation is given in Fig. 25.

In an attempt to use these models to predict the forming limits in upsetting of cylinders, calculations were performed on both the R-model and Z-model for values of  $K$  ranging between 0 and 2.0. Prestrain ( $\epsilon_0$ ) was taken as 0.1, and two different  $n$ -values (0.1 and 0.25) were used. Initial  $f_0$  values of 0.8, 0.95, and 0.99 were also used. Calculations were terminated when  $f$  became zero, which is taken as the limiting condition of fracture (Ref 39).

**The Cockcroft-Latham criterion** of fracture (Ref 40) is not based on a micromechanical model of fracture but simply recognizes that tensile stress and plastic deformation are the essential macroscopic ingredients of fracture. The Cockcroft-Latham criterion suggests that fracture occurs when the accumulated tensile strain energy reaches a critical value:

$$\int_0^{\epsilon} \sigma^* d\epsilon = C \quad (\text{Eq 17})$$

where  $\sigma^*$  is the maximum tensile stress;  $\epsilon$  is the equivalent strain; and  $C$  is a constant determined experimentally for a given material, temperature, and strain rate. This criterion is an outgrowth of the more general postulate by Freundenthal (Ref 41) that fracture occurs when the plastic work per unit volume reaches a critical value. Other variations of the basic concept have been proposed by Oh et al. (Ref 42), Brozzo et al. (Ref 43), and Bao and Weirzbicki (Ref 44). Gouveia et al. (Ref 45) showed by experiment and finite-element study that the Cockcroft-Latham criterion provided the best predictive capability. The Cockcroft-Latham criterion, by integrating the tensile plastic work over the entire metal-working process, accumulates the damage done

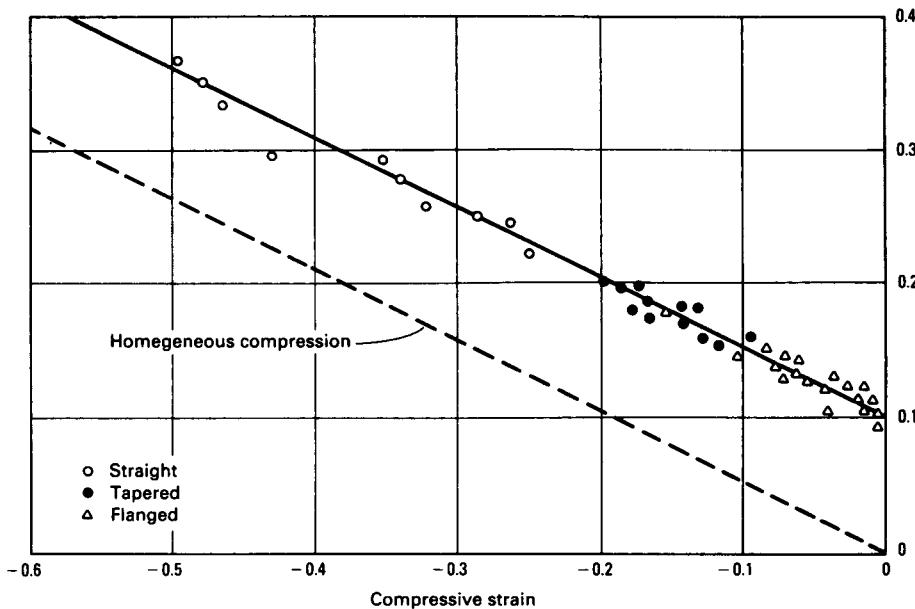


Fig. 19 Fracture locus for aluminum alloy 2024-T351 at room temperature

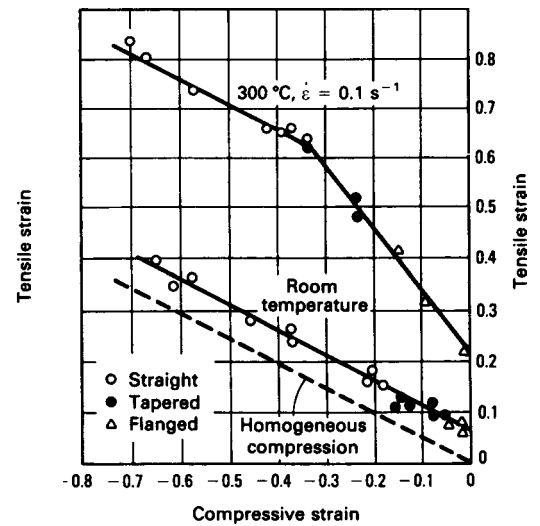
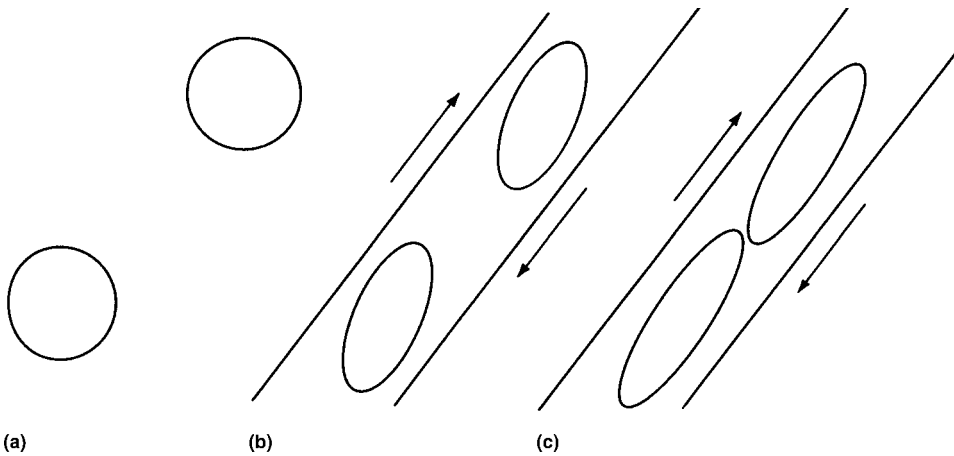
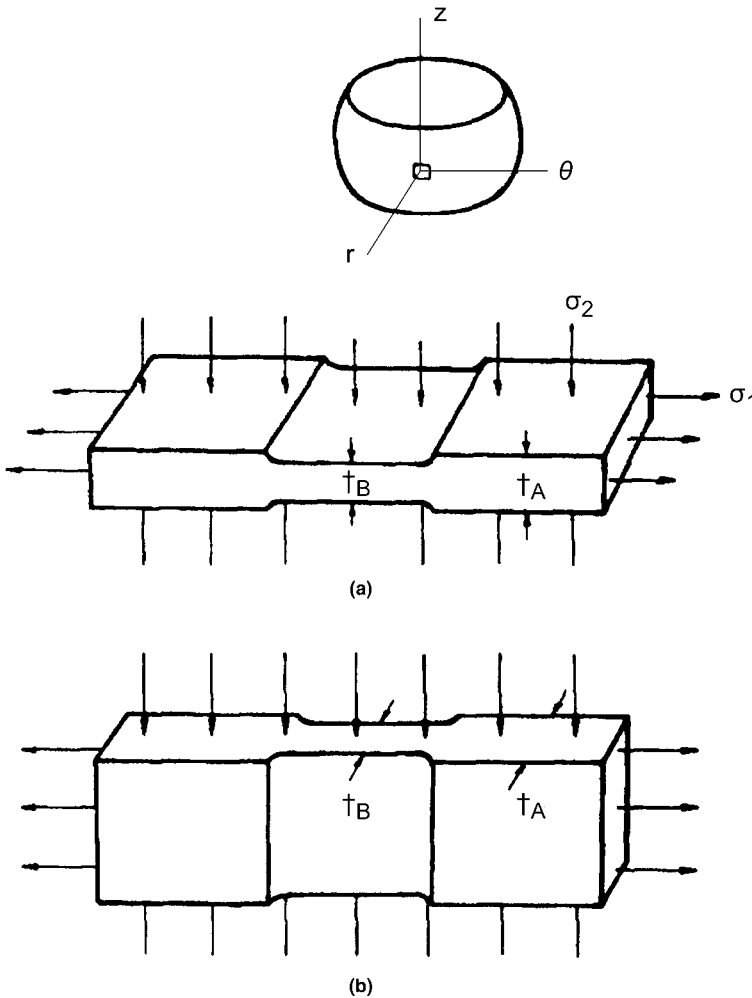


Fig. 20 Fracture locus for aluminum alloy 2024-T4 at room temperature and at 300 °C (570 °F).  $\dot{\epsilon} = 0.1 \text{ s}^{-1}$



**Fig. 21** McClintock model of void coalescence by shear from (a) initial circular voids, through (b) growth, and (c) void contact or coalescence.



**Fig. 23** Material elements used as models for plasticity analysis of localized thinning and fracture of materials. (a) R-model (b) Z-model

to the microstructure (microvoid formation, void growth and coalescence) by tensile stresses and plastic deformation so that when it reaches a critical value,  $C$ , fracture occurs.

**Extension of the Criterion to the Fracture Locus for Compression.** The Cockcroft-Latham criterion has been reformulated to provide a predicted fracture line for

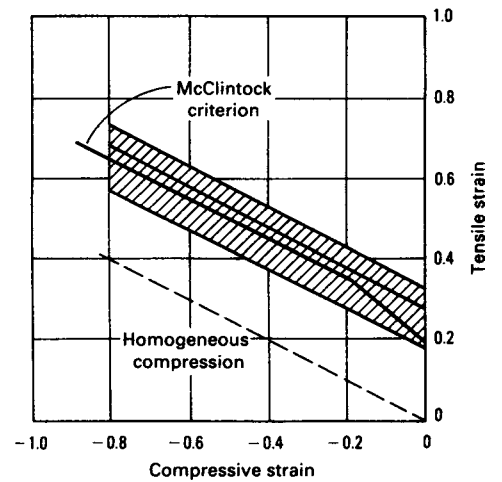


**Fig. 22** Fracture strain locus predicted by the McClintock model of void growth. The shaded area represents typical experimental fracture loci such as Fig. 18 to 20

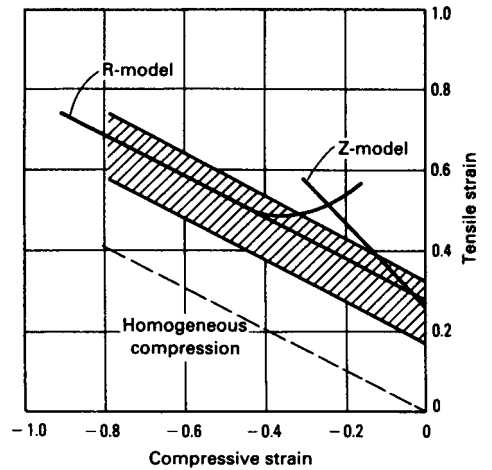


**Fig. 24** Fracture strain locus predicted by the model of localized thinning. The shaded area represents typical experimental fracture loci, such as Figs 18 to 20

comparison with the experimental fracture strain line.

This criterion was extended to cover the case of a simple compression. The strains involved in upsetting a cylinder—the basic test used in experimental determination of fracture lines—are illustrated in Fig. 26. In this case, the circumferential stress,  $\sigma_\theta$ , is the maximum tensile stress, that is,  $\sigma^*$  in Eq 17.

If the stress ratio is defined as:

$$r = \sigma_z / \sigma_\theta \tag{Eq 18}$$

and the imposed strain ratio is:

$$\alpha = -d\epsilon_z / d\epsilon_\theta \tag{Eq 19}$$

then from the Levy-Mises equations:

$$\alpha = (1 - 2r) / (2 - r) \tag{Eq 20}$$

$$\sigma^* = \sigma_\theta = \left[ \frac{\bar{\sigma}}{d\bar{\epsilon}} \right] \frac{d\epsilon_\theta}{(1-r/2)} \quad (\text{Eq 21})$$

Assuming the power strain-hardening law is valid during the deformation:

$$\bar{\sigma} = K\bar{\epsilon}^n \quad (\text{Eq 22})$$

where  $\bar{\sigma}$  is the equivalent stress,  $\bar{\epsilon}$  is the equivalent strain,  $K$  is the stress at  $\bar{\epsilon} = 1.0$ , and  $n$  is the strain-hardening exponent.

The relationship between equivalent strain and the individual strains can be written as:

$$\bar{\epsilon} = \left[ (\epsilon_r - \epsilon_z)^2 + (\epsilon_z - \epsilon_\theta)^2 + (\epsilon_\theta - \epsilon_r)^2 \right]^{1/2} \left[ \frac{\sqrt{2}}{3} \right] \quad (\text{Eq 23})$$

From this equation, and Eq 19,  $\bar{\epsilon}$  can be written in terms of  $\epsilon_\theta$  and  $\alpha$ . The expression involving  $\bar{\epsilon}$ ,  $\epsilon_\theta$ , and  $\alpha$  is:

$$\bar{\epsilon} = 2\epsilon_\theta [(1 - \alpha + \alpha^2)/3]^{1/2} \quad (\text{Eq 24})$$

From Eq 17, 21, and 24, the following equation was obtained:

$$\int_0^{\bar{\epsilon}} \sigma^* d\bar{\epsilon} = C = \left[ \frac{2k}{\sqrt{3}} \right] \left[ \frac{2}{\sqrt{3}} \right]^n \int_0^{\epsilon_{\theta f}} \left[ (1 - \alpha + \alpha^2)^{1/2} \epsilon_\theta \right]^n (2 - \alpha) d\epsilon_\theta \quad (\text{Eq 25})$$

The value of  $C$  can be determined from Eq 25 after integrating and solving for  $\epsilon_{\theta f}$ . For strain ratio  $\alpha = 0$ , the plane-strain case,  $\epsilon_{\theta f}$  is equal to the intercept of the fracture line,  $a$ . Then:

$$\epsilon_{\theta f} (\alpha = 0) = a = \left[ \frac{C}{k} \right]^{1/(1+n)} \cdot 3^{(n+2)/2(n+1)} \cdot \left[ \frac{1}{2} \right]^{1/(1+n)} \quad (\text{Eq 26})$$

where  $a$  is the intercept on the  $\epsilon_\theta$  axis of the fracture line,  $k$  is the stress at  $\bar{\epsilon} = 1.0$ , and  $n$  is the strain-hardening exponent.

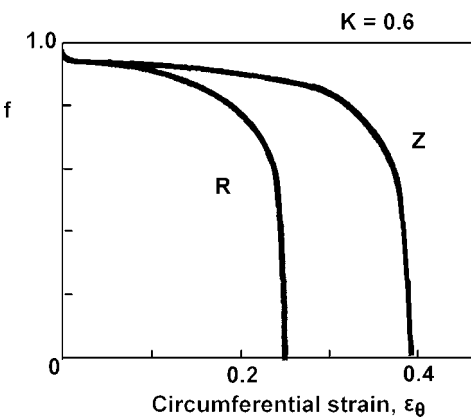


Fig. 25 Variation of  $f = t_A/t_B$  for the R-model and Z-model.  $K = 0.6$ ,  $f_0 = 0.99$ ,  $n = 0.25$

The value of the intercept,  $a$ , for various materials was determined experimentally. For 1020 steel and 1045 steel,  $a$  was found to be 0.32 and 0.29, respectively. Figure 27 shows that the fracture strain line predicted by the Cockcroft–Latham criterion, Eq 17, also is in reasonable agreement with the experimental results. The height of the predicted fracture line is determined by experiment, such as a tension test, rather than by speculation on a material inhomogeneity strength.

Figure 27 shows that the fracture strain line predicted by the Cockcroft–Latham criterion is also in reasonable agreement with experimental results. This criterion does not show the dual-slope behavior of the previous models and some actual materials. However, the correspondence between the Cockcroft–Latham criterion, the fracture model-based criteria, and the experimental data shows that all of the criteria are generally in agreement with the overall nature of surface strains at fracture in upset compression tests. In addition, the Cockcroft–Latham criterion (Eq 17) is the easiest to implement in a finite-element analysis code.

To be a truly useful fracture model, however, the criterion must be applicable to all conditions in metalworking processes, not just the surface fracture in compression tests. Mathematically, the criterion can be extended to three-dimensional stress states by imposing a pressure,  $P$ , on the free surface. This has the effect of applying a hydrostatic pressure,  $P$ , to all directions because, to maintain yielding and the same strain state, the other two stresses must increase by the magnitude  $P$  as well. Then, the forming-limit line becomes modified, as illustrated in Fig. 28. For superimposed pressure ( $P > 0$ ), the fracture line increases in height and its slope increases slightly. For superimposed tension ( $P < 0$ ), the height of the fracture line decreases and curves downward.

**The effect of hydrostatic pressure on fracture** has been studied extensively.

It has been shown that superimposed pressure increases fracture strain for various materials and test methods. Under high hydrostatic pressure, even brittle materials such as marble have been made to flow plastically.

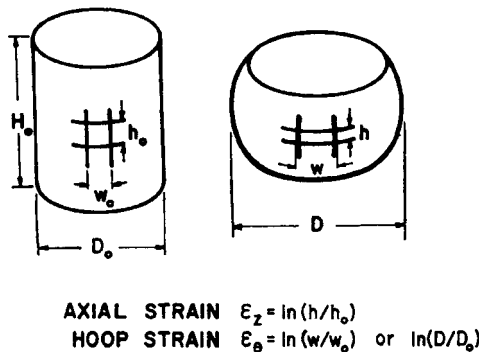


Fig. 26 Schematic diagram of upset test on cylindrical specimens. Surface strains at the equator are measured as shown.

The fracture model of Lee and Kuhn (Ref 39) can be modified to include hydrostatic pressure and thus determine its effect on the fracture strain line.

The Cockcroft–Latham criterion is modified to include the effects of superimposed hydrostatic pressure, because it has been shown that this criterion agrees well with experimental data for free surface fracture. The Cockcroft–Latham criterion (Eq 17) proposes that fracture will occur when the critical value,  $C$ , is reached.

Modifications to the criterion are made as follows. The deformation strain path for the region where fracture occurs is taken to be linear:

$$\alpha = \frac{d\epsilon_\theta}{d\epsilon_r} \quad (\text{Eq 27})$$

where  $d\epsilon_r$  and  $d\epsilon_\theta$  are increments of strain in the radial and circumferential directions, respectively. For each increment of deformation, the equivalent strain increment is:

$$d\bar{\epsilon} = (2/\sqrt{3})(\alpha^2 - \alpha + 1)^{1/2} d\epsilon_r \quad (\text{Eq 28})$$

Individual strain increments can be expressed in terms of stresses by means of the Lévy–Mises equations:

$$d\epsilon_\theta = \frac{d\bar{\epsilon}}{\bar{\sigma}} [\sigma_\theta - 1/2(\sigma_z + \sigma_r)] \quad (\text{Eq 29})$$

$$d\epsilon_r = \frac{d\bar{\epsilon}}{\bar{\sigma}} [\sigma_r - 1/2(\sigma_z + \sigma_\theta)] \quad (\text{Eq 30})$$

Equations 27, 29, and 30 are combined to form:

$$d\epsilon_r(2 - \alpha)/d\bar{\epsilon} = 3(\sigma_r - \sigma_z)/2\bar{\sigma} \quad (\text{Eq 31})$$

$$d\epsilon_r(1 - 2\alpha)/d\bar{\epsilon} = 3(\sigma_\theta - \sigma_z)/2\bar{\sigma} \quad (\text{Eq 32})$$

Substituting Eq 28 for the value of  $d\bar{\epsilon}$  yields:

$$\sigma_r = \bar{\sigma}(2 - \alpha)/[\sqrt{3}(\alpha^2 - \alpha + 1)^{1/2}] + \sigma_z \quad (\text{Eq 33})$$

$$\sigma_\theta = \bar{\sigma}(1 - 2\alpha)/[\sqrt{3}(\alpha^2 - \alpha - 1)^{1/2}] + \sigma_z \quad (\text{Eq 34})$$

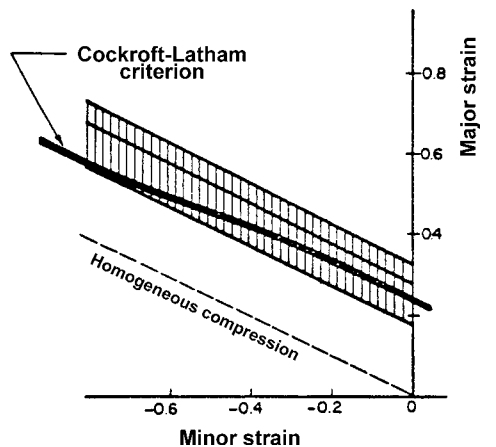


Fig. 27 Fracture strain locus predicted by the Cockcroft–Latham criterion. The shaded region represents the range of fracture lines determined experimentally.

It can be assumed that, as shown in Fig. 28, the  $z$ -plane is a free surface, and normal pressure  $P$  is applied to it. The effect of normal pressure  $P$  is to increase the pressure in all three directions; in other words, it increases the hydrostatic pressure level. Note that the first terms of Eq 33 and 34 are the same as those for deformations without an applied pressure for given value of  $\alpha$ , and  $\sigma_z$  appears as an addition in each equation.

From Eq 27 and 33, the Cockcroft-Latham criterion can be modified for superimposed hydrostatic pressure,  $P$ , by taking  $\sigma^* = \sigma_r$  as:

$$\begin{aligned}
 C &= \int_0^{\bar{\epsilon}_f} \sigma^* d\bar{\epsilon} = \int_0^{\bar{\epsilon}_f} (\sigma^* - P) d\bar{\epsilon} \\
 &= \int_0^{\bar{\epsilon}_f} \left\{ \bar{\sigma}(2 - \alpha) / [\sqrt{3}(\alpha^2 - \alpha + 1)^{1/2}] - P \right\} d\bar{\epsilon} \\
 &= \int_0^{\bar{\epsilon}_f} \left\{ \bar{\sigma}(2 - \alpha) / [\sqrt{3}(\alpha^2 - \alpha + 1)^{1/2}] \right\} d\bar{\epsilon} \\
 &\quad - \int_0^{\bar{\epsilon}_f} P d\bar{\epsilon} \\
 &= \int_0^{\bar{\epsilon}_{rf}} \left( \frac{2K}{3} \right) \left( \frac{2}{\sqrt{3}} \right)^n (2 - \alpha) [(\alpha^2 - \alpha + 1)^{1/2}]^n \epsilon_r^n \\
 &\quad - d\epsilon_r - P \int_0^{\bar{\epsilon}_{rf}} \frac{2}{\sqrt{3}} (\alpha^2 - \alpha + 1) d\bar{\epsilon}_r \\
 &= \left( \frac{2K}{3} \right) \left( \frac{2}{\sqrt{3}} \right)^n (2 - \alpha) (\alpha^2 - \alpha + 1)^{n/2} \frac{1}{n+1} \epsilon_{rf}^{n+1} \\
 &\quad - P \frac{2}{\sqrt{3}} (\alpha^2 - \alpha + 1)^{1/2} \epsilon_{rf}
 \end{aligned}
 \tag{Eq 35}$$

where  $\epsilon_{rf}$  is the radial strain at fracture.

For the model material under study, from previous experimental data for  $K$ ,  $n$ , and  $\epsilon_{rf}$  at  $\alpha = 0$  (plane strain),  $C$  was calculated. Then,  $\epsilon_{rf}$  was calculated for various values of  $\alpha$  between 0 and 2 and  $P$  by an iterative method.

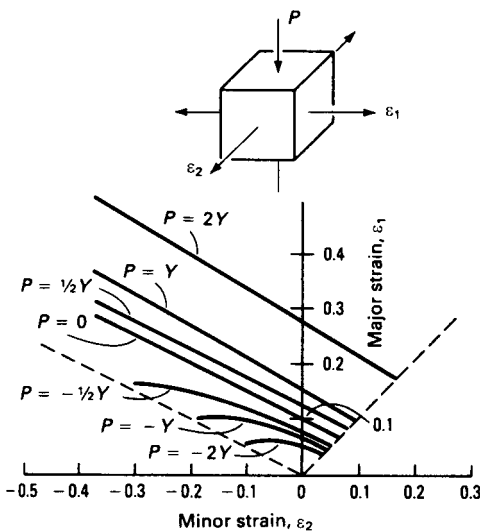


**Fig. 28** Movement of the fracture strain line due to superimposed hydrostatic stress. Applied stress is represented in terms of multiples of the yield strength,  $Y$ . Negative values of  $P$  indicate hydrostatic tension. Calculations are based on a modification of the Cockcroft-Latham criterion.

The results are shown in Fig. 29 for various hydrostatic pressure levels (in relation to yield strength,  $Y$ ). As the level of hydrostatic pressure increases, the intercept increases and the slope of the fracture line increases above one-half. This is consistent with empirical results.

The measured surface strains and hydrostatic pressure levels determined by the viscoplasticity method were combined with theoretical forming-limit diagrams developed from the Cockcroft-Latham criterion.

As shown in Fig. 30, at 45% height strain for unlubricated specimens, strains are below the fracture line, and no fracture, in fact, was observed. For the lubricated specimens, the strains are above the fracture line, and fractures were observed.

To evaluate the Cockcroft-Latham criterion for nonfree surface fractures, the double-extrusion forging process (recall Fig. 6) was carried out with a split billet containing a deformation grid (Fig. 31). Measurements of the grid displacements on this midplane were made at several increments of deformation, and the viscoplasticity method (Ref 10) was used to calculate the strains and hydrostatic pressure at the midpoint. The hydrostatic stress state at the center of the specimen is initially compressive and then reverses, becoming tensile as the flange thickness is reduced and metal flows into the opposing hubs. Meanwhile, the strains at the center are increasing monotonically as deformation progresses. This is illustrated in Fig. 32 by the steps 0, 1, 2, and 3. As deformation proceeds, the strains at the center increase, but the hydrostatic pressure is also increasing, so the fracture line moves upward. Then, as the flange thickness approaches one-half of the hub base diameter (die orifice diameter), the hydrostatic stress becomes tensile. At this point, the fracture line decreases in height, but the strains at the center continue to rise and cross the fracture line, coinciding with the formation of the central

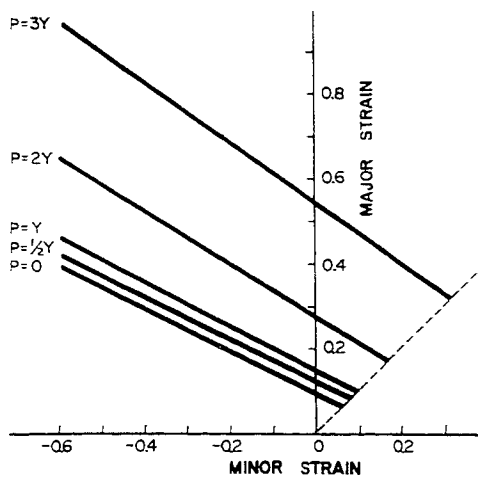


**Fig. 29** Fracture strain lines as predicted by the Cockcroft-Latham criterion in quadrants one and two of the strain plane;  $P$  is the superimposed pressure.

burst. The calculated hydrostatic tension at fracture was 0.3 yield stress ( $Y$ ). This approach could be used for predicting central burst in drawing and extrusion to provide a material-dependent criterion, as opposed to the more simplistic upper-bound and tensile stress criteria described previously.

Frequently, cracks occur during forging on surfaces that are in contact with the dies and then move around a die corner (Fig. 33). From the observation of a variety of such defects, it appears that a common characteristic is an abrupt change in frictional shear traction distribution in the region of the crack.

A technique for studying die contact surface cracks was developed by means of a disk compression test using dies having a rough surface in the central region and a smooth surface in the outer region. Figure 34 shows the top view of a 6061 aluminum alloy disk compressed between such dies. In the transition region between the rough central die surface and the smooth outer region, radial cracks initiate and propagate outward. Such cracks occurred at approximately 30% reduction when the smooth outer region was lubricated with a synthetic fluorine-containing resin. The cracks occurred at approximately 45% reduction when grease lubrication was used in the outer smooth region. No cracks occurred even for very large reductions when the smooth outer region was not lubricated.

Grid marks placed on the die contact surface of the disks were used to measure the distribution of surface strains in the radial direction. Figure 35 gives an example of such measurements. In the rough central region, the strains are zero, while in the smooth outer region, the strains are equal and constant. In the transition, however, the circumferential strain,  $\epsilon_\theta$ ,

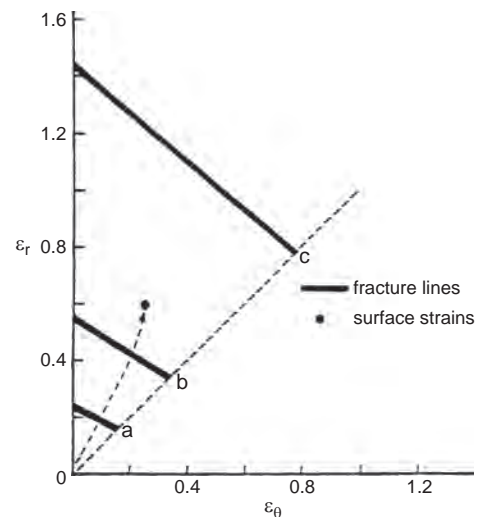


**Fig. 30** Resulting strains at the transition at 45% deformation and fracture lines for each case of friction condition. The resulting strain crossed the fracture lines for synthetic fluorine-v containing resin- (a) and grease-lubricated (b) cases but is below the fracture line for the unlubricated case (c).

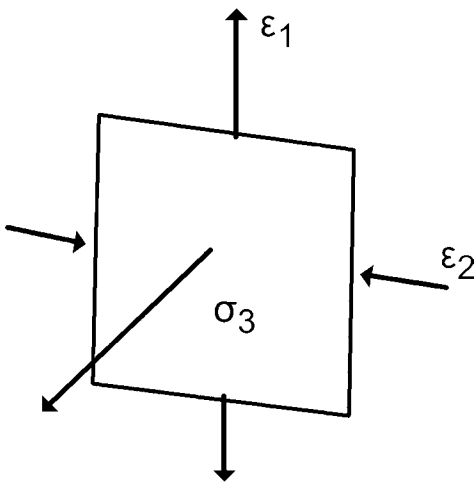
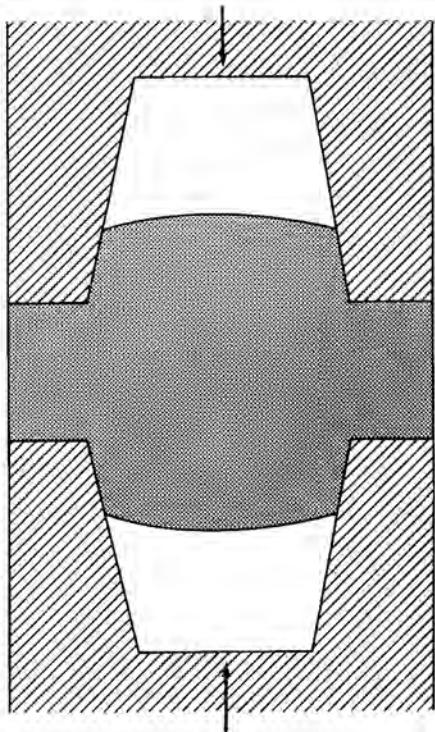
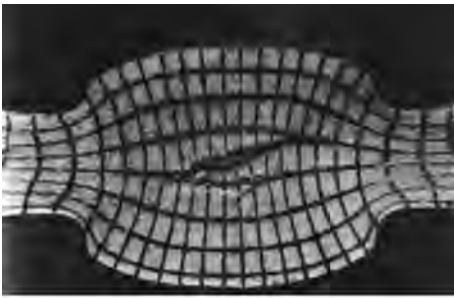


**Fig. 31** Internal fracture during the double-extrusion forging of aluminum alloy 6061. Grid deformations on the middle longitudinal plane are shown. The stress-strain states are defined by the insert,  $\sigma_3$  is perpendicular to the plane of the schematic bulging the free surface.

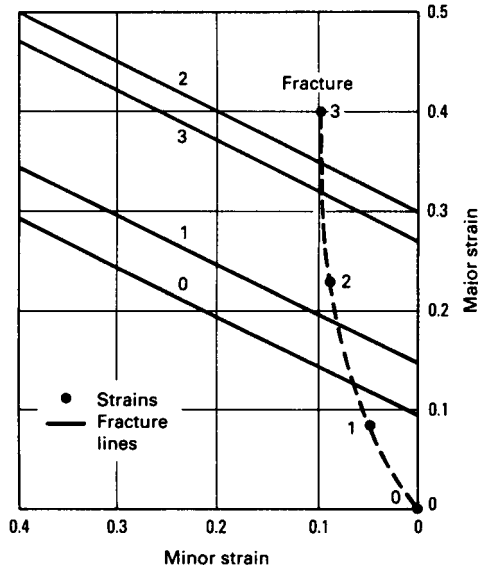
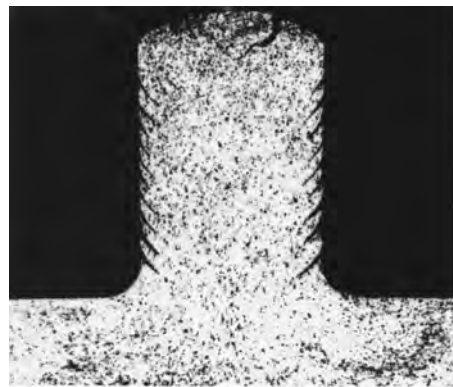
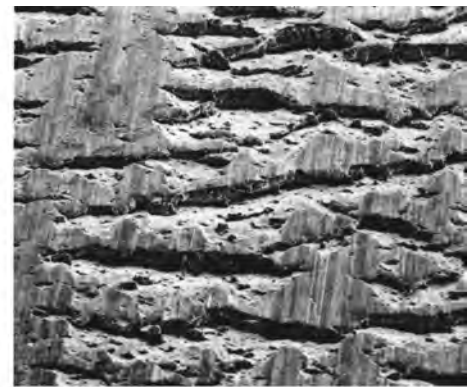


**Fig. 32** Progression of surface strains and fracture line at the central internal location of the double-extrusion forging shown in Fig. 31. The fracture line rises from 0 to 1 to 2 as internal pressure increases and then falls to point 3 as internal stress becomes tensile. Meanwhile, the strains at the center continue to rise and cross the fracture line at the deformation stage in which internal fracture occurs.



(a)



(b)

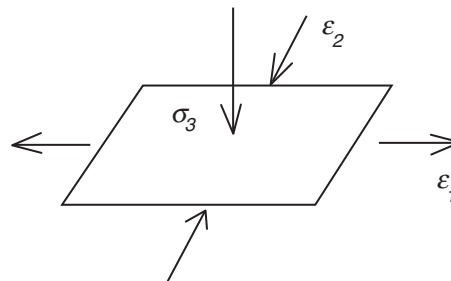


**Fig. 33** Die contact surface cracking during forging extrusion of aluminum alloy powder compact. (a) Cross section. (b) Normal to vertical rib surface. Note also the cracks at the top free surface. The cracks form as material flows from the flange area beneath the punch into the die cavity. Stress-strain states are defined in insert,  $\sigma_3$  is normal to the free surface.

jumps abruptly from zero to its constant value in the outer region, and the radial strain,  $\epsilon_r$ , overshoots to a very high value before returning to its constant value in the smooth outer region. The strains shown in Fig. 35 were the same regardless of the friction condition in the smooth outer region. Therefore, fractures in the transition region occur because of the combination of large tensile surface strains and low hydrostatic stress state. This explains the occurrence of cracks at low reduction when a synthetic fluorine-containing resin is used, and no occurrence of fracture when no lubricant is used. The synthetic fluorine-containing resin, having a near-zero friction coefficient, results in very low radial back pressure on the transition region, while grease and no lubricant provide progressively larger back pressures.

By means of viscoplasticity analysis (Ref 10), the stresses were determined at the contact surface in the vicinity of the transition region. The resulting normal die pressure plus the surface radial and circumferential strains define the stress and strain states in the transition region and can be illustrated on a forming-limit diagram. Figure 36 shows the change in surface strains and the increase in the fracture line due to increasing normal pressure during compres-

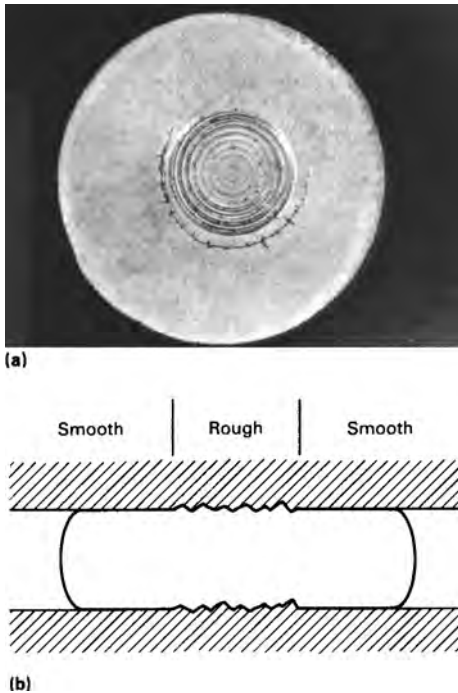


**Fig. 34** (a) Top view of aluminum alloy 6061 disk compressed between dies. (b) Cracks form at the transition region between rough and smooth areas of the die.

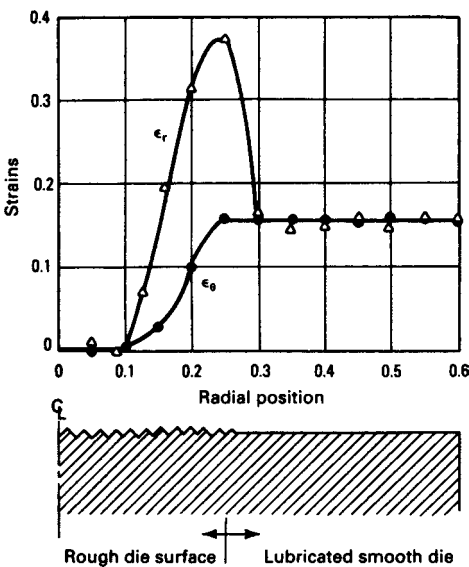


**Fig. 35** Radial variation of contact surface strains after 30% compression of the disk shown in Fig. 34

sion of a disk with grease lubricant in the outer region (indicated by the increments of reduction to 45%). The fracture line increases due to increasing pressure at a slower rate than the strains increase, and at 45% reduction, the strain path exceeds the fracture line, and cracks are observed. For a synthetic fluorine-containing resin lubricant, the crossover occurs at approximately 30% reduction, while in the case

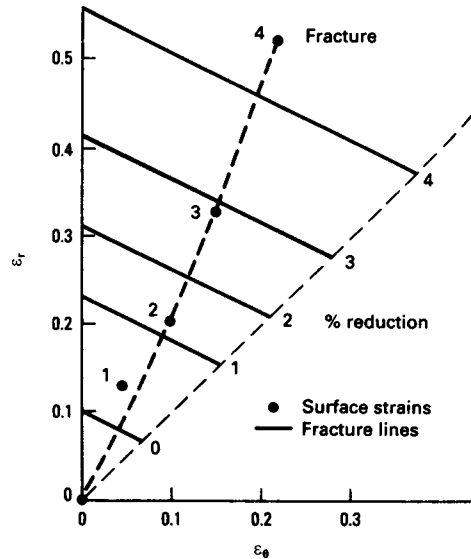


**Fig. 36** Progression of surface strains and fracture line at the transition region between rough and smooth zones of the compressed disk shown in Fig. 35. Points 1, 2, 3, and 4 represent 10, 20, 30, and 45% reduction, respectively.

of no lubricant, the fracture line moves progressively away from the strain path.

While these are crude measurements taken at only a few deformation steps, Fig. 32 and 36 do provide some experimental validation of the Cockcroft-Latham fracture line (Fig. 28), and it would be expected to provide accurate predictions of fracture at any location in a workpiece. A true test of the criterion is to embed it in finite-element codes for prediction of fracture under a variety of metalworking processes. The criterion has become integral to large deformation codes such as DEFORM and MSC.MARC. As a simple example, Fig. 37(a) shows the prediction of fracture at the centerline of a round billet compressed between parallel flat dies (Ref 46, 47), similar to the geometry shown in Fig. 38. The damage value is highest at the center and reaches the critical value for fracture. Figure 37(b) shows the same billet between a three-die arrangement. The new deformation geometry reduces the damage level below the critical value for the material.

A further example of application of the Cockcroft-Latham criterion, the DEFORM code for simulation of plastic deformation processes, was applied to axisymmetric extrusion, as shown in Fig. 39, in which three separate reductions are taken (Ref 48). The Cockcroft-Latham criterion was incorporated with the detailed calculation of stresses and strains throughout the extrusion process to indicate regions in which high microstructural damage occurred. It is clear that as the damage increases, central burst is predicted to occur after the third reduction, which is commonly observed.

Another example, shown in Fig. 40, involves formation of an axisymmetric part formed by

back extrusion. Circumferential cracks form on the inside surface of the part at the location identified in Fig. 41 by point P2. Note that P2 is originally under the punch but then moves around the punch radius and up the sidewall of the part, similar to the example shown in Fig. 33. The calculated damage, according to the Cockcroft-Latham criterion embedded in DEFORM, is shown for P2 in Fig. 42. Note that the damage is very low as long as P2 is under the punch but increases rapidly as soon as it goes around the punch corner and separates from the punch. This is similar to the experimental measurements and calculations carried out in Fig. 34 through 36.

**Testing precautions** must be used in applying the Cockcroft-Latham criterion through finite-element codes. While the codes are capable of producing faithful reproductions of the distributions of stress and strain throughout the workpiece during a metalworking process, accurate prediction of fracture-occurrence location and time still depends on a faithful representation of the fracture phenomenon through the material factor,  $C$ . One approach is to use the upset compression test to establish a fracture line for the material, as in Fig. 18–20, and then perform finite-element analyses of the tests to establish the value of tensile plastic work at which the fractures occur, that is, the value of  $C$ .

When considering workability tests, it is important to recognize that fractures initiate in localized regions where interaction between the stress and strain states and the material structure reaches a critical level. Orientation, shape, and volume fraction of inclusions and other microstructural inhomogeneities have a dominant effect on the fracture process. Therefore, it is critically important that workability test specimens contain material having the same microstructural features as the material in the localized, potential fracture regions of the actual process.

Specifically, when evaluating a workpiece for surface fractures, the test specimens used to evaluate  $C$  must have surfaces that contain the as-received surface of the workpiece under consideration. The as-received surface may contain laps, seams, a decarburized layer, and so on, which affect fracture initiation. By the same argument, evaluation of material for internal fractures such as central burst must involve test specimens taken from the middle of the workpiece, where, for example, segregation of second phases may have occurred. In this case, bending tests wherein the convex bending surface coincides with the centerline of the workpiece may be the preferred test geometry. Furthermore, because of possible anisotropy effects, orientation of the critical stresses with respect to any inclusion alignment must be the same in the test specimens as it is in the actual process and material of interest. All of these considerations place great importance on correct selection of the test specimen material

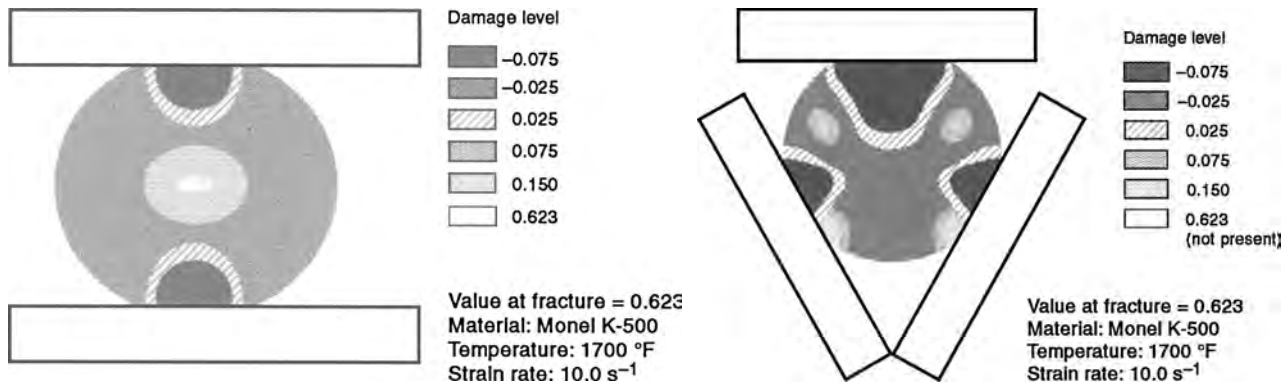


**Fig. 37** Damage level modeled for round billet. (a) Model showing damage values corresponding to the process used to manufacture the part shown in Fig. 38. (b) Model showing damage values obtained after modification to the platen used to manufacture the part shown in Fig. 38



**Fig. 38** Plasticine ingot representing side pressing of a K-Monel ingot. Hard beads have been embedded to illustrate the presence of tensile stresses at the center of the ingot. Damage seen is directly related to the tensile stresses.

and geometry to provide a true representation of the tensile plastic energy to fracture. For this purpose, bending as well as compression tests must be considered in preference to tensile testing, because the failure in a tension test occurs by necking instability and involves material that is at the center of the specimen rather than at the surface.

## Fundamental Fracture Models

In the current state of fracture prediction in metalworking processes, computer models provide robust simulations of the deformation, stresses, and strains throughout the workpiece, but the material fracture characteristics must be input from data gathered through properly selected test specimens and procedures. New efforts are being made to provide a prediction of the fracture characteristics of a material from knowledge of its microstructural and crystallographic details.

One approach involves the application of finite-element analysis in a multiscaled approach (Ref 49). Unit cell models are used at each scale to discern the micromechanics of the fracture process. The three scales (Fig. 43) include the atomic distance to assess debonding

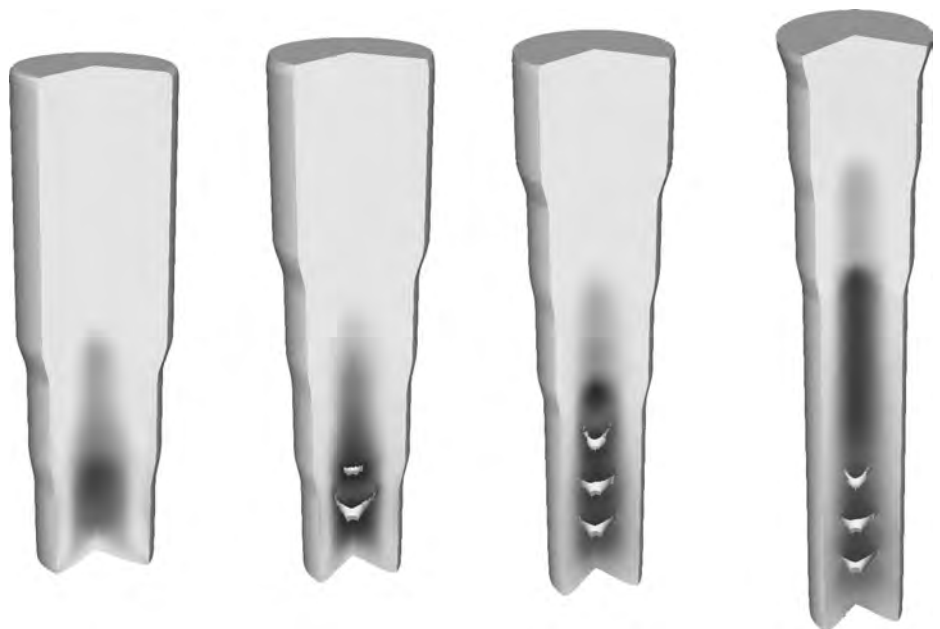


**Fig. 39** Prediction of internal damage and central burst by the Cockcroft criterion in the DEFORM large deformation finite element program. Source: Ref 43

of particles, the nanometer scale of microvoid-nucleating secondary particles, and the micrometer scale of primary void-forming inclusions. One difficulty with the approach involves the distribution of particles. Fracture generally begins at the weakest link of the material, which would be the location of closely spaced particles. For this reason, modeling is performed around clusters of particles having a higher density of particles than the average throughout the material. Another problem involves accurate representation of debonding at particle-matrix interfaces. A first-principles calculation can be used to determine the bonding energy at the interfaces. Then, the particle-matrix interface is modeled by the finite-element code as one-dimensional cohesive elements. Figure 44 shows an example of microvoid formation and coalescence in two-dimensional shear deformation. A more long-

range approach involves application of first-principles-based molecular dynamics calculations to simulate the generation of dislocations around particles, leading to separation of the matrix from the particle and void formation (Ref 50). Figure 45 illustrates a typical sequence of events in the vicinity of a particle.

## REFERENCES

1. G. Sachs, *Fundamentals of the Working of Metals*, Pergamon Press, 1954
2. B.I. Edelson and W. M. Baldwin, *Trans. ASM*, Vol 55, 1962, p 230-250
3. P.W. Bridgman, *Studies in Large Plastic Flow and Fracture*, Harvard Press, 1964
4. G.W. Pearsall and W.A. Backofen, "Frictional Boundary Conditions in Plastic Compression," Paper 62-Prod-2, ASME, 1962



**Fig. 40** Photograph of a back extruded part. Note the severe circumferential fracture (dark area) and die underfill (below dark area) on the inside diameter (ID).

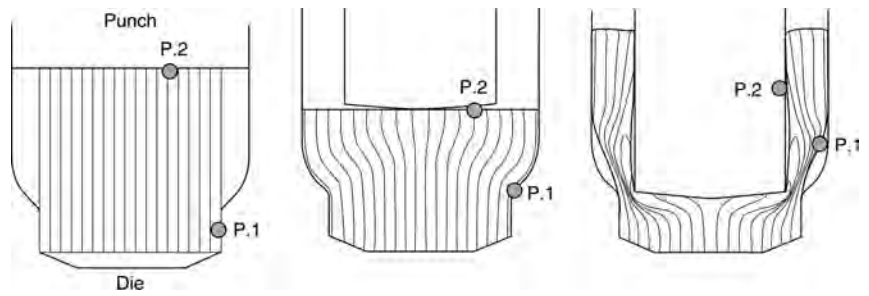


**Fig. 41** Flowlines for the forming of the component. Note that point P2 moves from beneath the punch into the wall of the part.

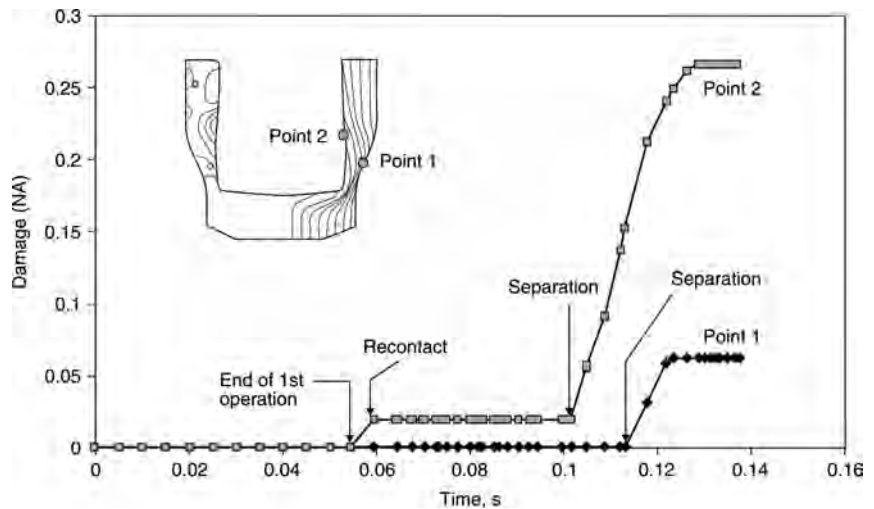


**Fig. 42** Point tracking the damage factor of two points on the surface of the component using the Cockcroft criterion in the DEFORM large deformation finite element program.

- M.C. Shaw, Surface Conditions in Deformation Processes, *Fundamentals of Deformation Processing*, Ninth Sagamore Army Materials Research Conference, Syracuse University Press, 1964, p 107–130
- I.Y. Tarnovskii, A.A. Pozdeyev, and V.B. Lyashkov, *Deformation of Metals during Rolling*, Pergamon Press, 1965
- C.T. Yang and E.G. Thomsen, Plastic Flow in a Lead Extrusion, *Trans. ASME*, Vol 75, 1953, p 575–579
- S. Kalpakcioglu, An Experimental Study of Plastic Deformation in Power Spinning, *CIRP Annales*, Vol 10, 1962
- A.S. Kao and H.A. Kuhn, Physical Modeling of Ductile Fracture in Metalforming Process, *J. Eng. Mater. Technol.*, Vol 112, 1990, p 302–308
- E.G. Thomsen, C.T. Yang, and S. Kobayashi, *Mechanics of Plastic Deformation in Metal Processing*, The Macmillan Company, 1965, p 178
- T. Erturk, H.A. Kuhn, and A. Lawley, Forging of Metal-Matrix Composites—Forming Limit Criteria, *Met. Trans.*, Vol 5, 1974, p 2295–2303
- H. Kudo, An Upper-Bound Approach to Plane-Strain Forging and Extrusion, *Int. J. Mech. Sci.*, Vol 1, 1960, p 57
- W. Johnson and H. Kudo, *The Mechanics of Metal Extrusion*, Manchester University Press, 1962
- B. Avitzur, *Metal Forming—Processes and Analysis*, McGraw-Hill, 1968
- W.M. Evans and B. Avitzur, “Die Design for Drawing Extrusion,” Paper MF67-582, Society of Manufacturing Engineers, 1967
- B. Avitzur, “Strain Hardening and Strain Rate Effects in Plastic Flow Through Conical Converging Dies,” Paper 66-Prod-17, American Society of Mechanical Engineers, 1966
- Z. Zimmerman, H. Darlington, and E.H. Kottcamp, Jr., Selection of Operating Parameters to Prevent Central Bursting during Cold Extrusion, *Mechanical Working and Steel Processing*, TMS, 1970, p 405
- R. Hill, On the Inhomogeneous Deformation of a Plastic Lamina in a Compression Test, *Philos. Mag.*, Vol 41, 1950, p 733
- R. Hill, *Mathematical Theory of Plasticity*, Oxford Press, 1950, p 128
- H.C. Rogers and L.F. Coffin, “Investigation of the Nature of Structural Damage in Metal-Forming Processes,” Final report, Contract N0w-66-0546-d, Naval Air Systems Command, June 1967
- R. Wright, Workability and Process Design in Extrusion and Drawing, *Handbook of Workability and Process Design*, ASM International, 2003, p 316–321
- A. Chaudhary and S. Vaze, Design Optimization for Dies and Preforms, *Metalworking: Bulk Forming*, Vol 14A, *ASM Handbook*, ASM International, 2005, p 640–644
- W.A. Backofen, Some Unifying Aspects of Deformation Processing, *Fundamentals of Deformation Processing*, Ninth Sagamore Army Materials Research Conference, Syracuse University Press, 1964, p 1–10
- H.A. Kuhn, G.E. Dieter, and S.L. Semiatin, Workability and Process Design—An Introduction, *Handbook of Workability and Process Design*, ASM International, 2003, p 3–20
- K.E. Puttick, Ductile Fracture in Metals, *Philos. Mag.*, Vol 4, 1959, p 964
- G.E. Dieter, Introduction to Ductility, *Ductility*, ASM International, 1967, p1–27
- H.C. Rogers, The Mechanism of Crack Propagation in Ductile Metals, *Acta Metall.*, Vol 7, 1959, p 750
- H.A. Kuhn, Workability Theory and Application in Bulk Forming Processes, *Handbook of Workability and Process Design*, ASM International, 2003, p 172–187
- H. Kudo and K. Aoi, Effect of Compression Test Condition upon Fracturing of a Medium Carbon Steel—Study on Cold-Forgeability Test: Part II, *J. Jpn. Soc. Technol. Plast.*, Vol 8, 1967, p 17–27
- S. Kobayashi, Deformation Characteristics and Ductile Fracture of 1040 Steel in Simple Upsetting of Solid Cylinders and Rings, *J. Eng. Ind. (Trans. ASME)*, 1970, p 391–399
- P.F. Thomason, Tensile Plastic Instability and Ductile Fracture in Uniaxial Compression Tests, *Int. J. Mech. Sci.*, Vol 11, 1968, p 187–202

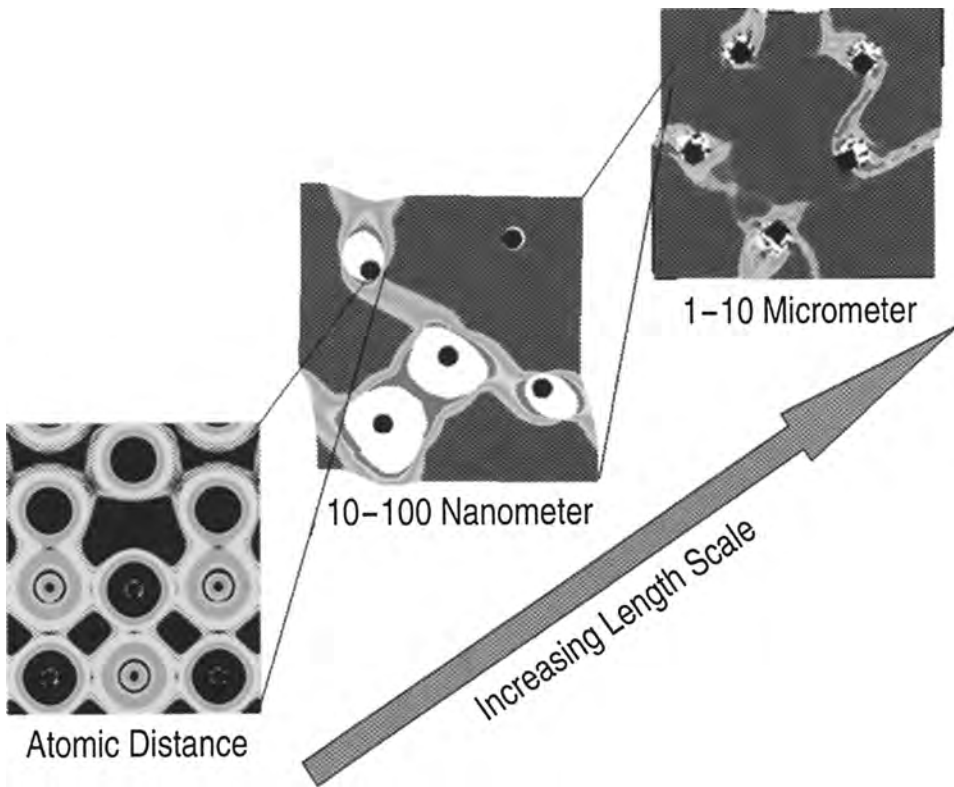


**Fig. 43** Three scales of fracture models in a comprehensive approach to simulation of ductile fracture by void formation, growth, and coalescence. Source: Ref 44

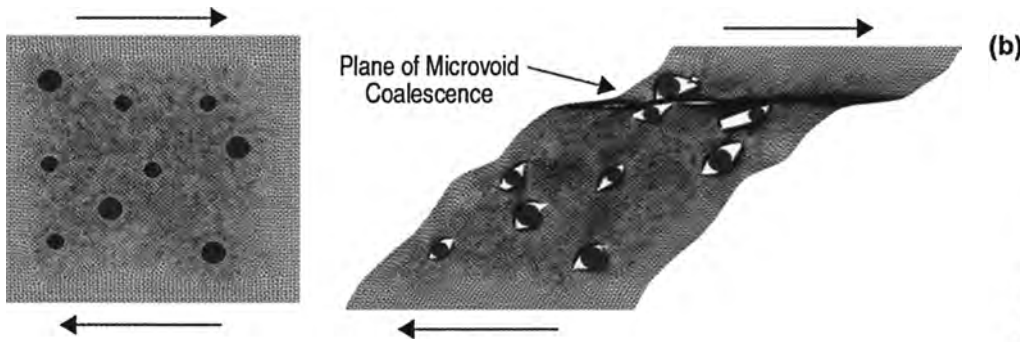


**Fig. 44** Simulated formation of microvoids and their growth and coalescence. Source: Ref 44

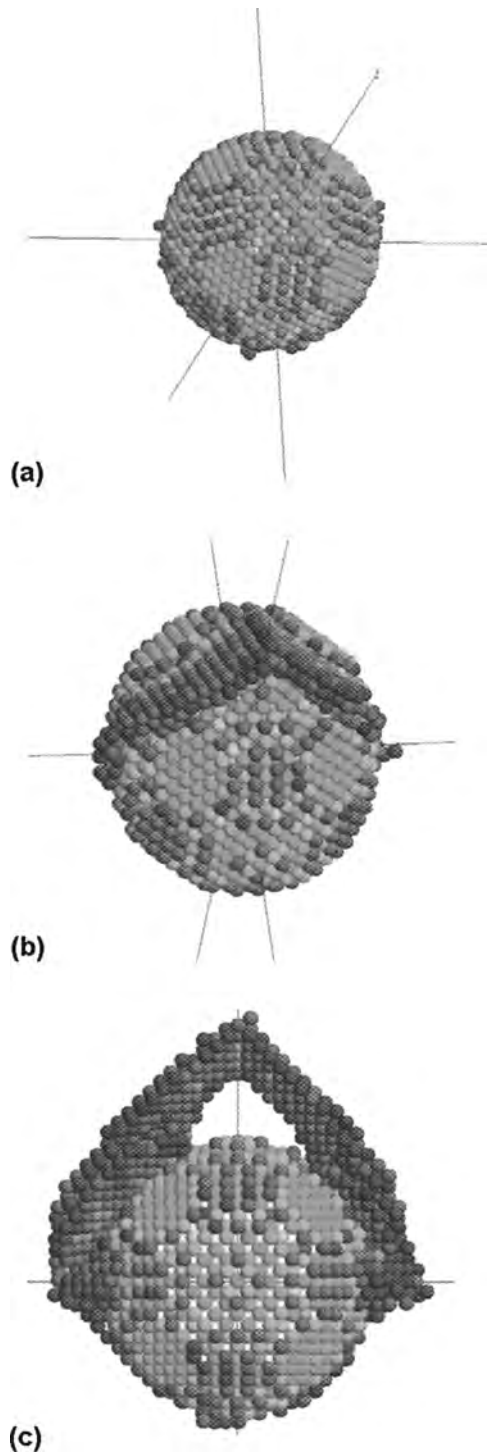


**Fig. 45** Molecular dynamics modeling of dislocation motion and void formation in the vicinity of a hard particle. Source: Ref 45

- |   |   |  |
|---|---|--|
| <p>32. H.P. Ganser, A.G. Atkins, O. Kolednik, F.D. Fischer, and O. Richard, Upsetting of Cylinders: A Comparison of Two Different Damage Indicators, <i>J. Eng. Mater. Technol.</i>, Vol 123, 2001, p 94–99</p> <p>33. Y. Bao and T. Wierzbicki, A Comparative Study on Various Ductile Crack Formation Criteria, <i>J. Eng. Mater. Technol.</i>, Vol 126, 2004, p 314–324</p> <p>34. H.A. Kuhn, P.W. Lee, and T. Erturk, A Fracture Criterion of Cold Forging, <i>J. Eng. Mater. Technol. (Trans. ASME)</i>, Vol 95, 1973, p 213–218</p> <p>35. F.A. McClintock, A Criterion for Ductile Fracture by the Growth of Holes, <i>J. Appl. Mech.</i>, Vol 33, 1968, p 363–371</p> | <p>36. J. Rice and D. Tracey, On the Ductile Enlargement of Voids in Triaxial Stress Fields, <i>J. Mech. Phys. Solids</i>, Vol 17, 1969, p 201–217</p> <p>37. Z. Marciniak and K. Kuczynski, A Model of Localized Thinning in Sheet Metal-forming, <i>Int. J. Mech. Sci.</i>, Vol 9, 1967, p 609</p> <p>38. H.A. Kuhn and P.W. Lee, Strain Instability Leading to Fracture at the Free Surface of Upset Cylinders, <i>Metall. Trans.</i>, Vol 2, 1971, p 3197–3202</p> <p>39. P.W. Lee and H.A. Kuhn, Fracture in Cold Upset Forging—A Criterion and Model, <i>Metall. Trans.</i>, Vol 4, April 1973, p 969–974</p> | <p>40. M.G. Cockcroft and D.J. Latham, Ductility and the Workability of Metals, <i>J. Inst. Met.</i>, Vol 96, 1968, p 33–39</p> <p>41. A.M. Freudenthal, <i>The Inelastic Behavior of Solids</i>, John Wiley &amp; Sons, 1950</p> <p>42. S.I. Oh., C.C. Chen, and S. Kobayashi, Ductile Fracture in Axisymmetric Extrusion and Wire Drawing: Part 2—Workability in</p> |
|---|---|--|

- Extrusion and Drawing, *J. Eng. Ind. (Trans. ASME)*, Vol 101 (No. 1), p 3644
43. P. Brozzo, B. Deluca, and R.A. Rendina, A New Method for the Prediction of the Formability Limits of Metal Sheets, *Proceedings of the Seventh Biennial Conference on Sheet Metal Forming and Formability*, International Deep Drawing Research Group, Amsterdam, 1972
  44. Y. Bao and T. Wierzbicki, On the Cut-Off Value of Negative Triaxiality for Fracture, *Eng. Fract. Mech.*, Vol 72, 2005, p 1049–1069
  45. B. Gouveia, J. Rodrigues, and P. Martins, Ductile Fracture in Metalworking Experimental and Theoretical Research, *J. Mater. Process. Technol.*, Vol 101, 2000, p 52–63
  46. D. Zhao, J.P. Bandstra, and H.A. Kuhn, A New Fracture Criterion for Metalworking Processes, *Concurrent Engineering Approach to Materials Processing*, S.N. Dwivedi, A.J. Paul, and F.R. Dax, Ed., TMS, 1992, p 107–119
  47. M.L. Tims, J.D. Ryan, W.L. Otto, and M.E. Natishan, Crack Susceptibility of Nickel-Copper Alloy K-500 Bars during Forging and Quenching, *Proc. First Int. Conf. on Quenching and Control of Distortion*, ASM International, 1992, p 243–250
  48. S.I. Oh, J. Walters, and W.T. Wu, Finite-Element Method Applications in Bulk Forming, *Metalworking: Bulk Forming*, Vol 14A, *ASM Handbook*, ASM International, 2005, p 615–639
  49. F.J. Vernerey, C. McVeigh, W.K. Liu, B. Moran, D. Tewari, D.M. Parks, and G. Olson, The 3-D Computational Modeling of Shear-Dominated Ductile Failure in Steel, *J. Met.*, Dec 2006, p 45–51
  50. M.A. Myers, S. Traiviratana, V.A. Lubarda, D.J. Benson, and E.M. Bringa, The Role of Dislocations in the Growth of Nanosized Voids in Ductile Failure of Metals, *J. Met.*, Feb 2009, p 35–41